Active aeroelastic flutter control of supersonic smart variable stiffness composite panels using layerwise models

Composite Structures 343 (2024) 118287

Contents lists available at ScienceDirect

Composite Structures

journal homepage: www.elsevier.com/locate/compstruct

Active aeroelastic flutter control of supersonic smart variable stiffness composite panels using layerwise models

J.A. Moreira [a,*], F. Moleiro [a], A.L. Araújo [a], A. Pagani [b]

[a] IDMEC, Instituto Superior Tecnico, Universidade de Lisboa, Av. Rovisco Pais 1, Lisboa, 1049-001, Portugal
[b] MUL2, Department of Mechanical and Aerospace Engineering, Politecnico di Torino, Corso Duca degli Abruzzi 24, Torino, 10129, Italy

ARTICLE INFO

Keywords:
Aeroelastic control
Panel flutter
Piezoelectric composite panels
Variable stiffness composites
Layerwise theory

ABSTRACT

This work focuses on the layerwise finite element modelling and active aeroelastic flutter control of smart variable stiffness laminated composite panels with surface bonded piezoelectric layers/patches under supersonic airflow. The proposed aero-electro-elastic models make use of the First- and Third-order Shear Deformation Theories, along with a linear through-thickness distribution of the electric potential, whereas the effect of the supersonic airflow is described by the First-order Piston Theory. Numerical applications of simply supported smart composite panels with either curvilinear or unidirectional fibres are provided for the accuracy assessment of the proposed models predictive capabilities, considering various side-to-thickness ratios and control conditions. The effect of proportional control on the aeroelastic flutter response is discussed for both airflow along the x-axis and yawed airflow, in addition to three different placement configurations of the piezoelectric patches.

1. Introduction

Smart materials with adaptive multifunctional capabilities are emerging as a promising structural design technology for advanced engineering systems. Among different types of smart materials, such as magnetostrictive materials and shape memory alloys, piezoelectric materials are a well-known suitable choice for active vibration control, noise attenuation, and structural health monitoring, as the direct and converse piezoelectric effects provide sensing and actuation capabilities to the structure [1,2]. In the context of active vibration control, aeroelastic vibrations and aeroelastic instabilities (e.g. subsonic wing flutter and supersonic panel flutter) are indeed a particular case of interest where the active control technology and smart structures have found success in pushing forward the aeroelastic performance [3–6] and reducing the damage of aero-structural components [7]. However, the proper modelling of smart composite laminates with piezoelectric sensor and actuator layers relies mostly on the accurate prediction of the through-thickness inhomogeneity of material properties, including the coupled electromechanical response behaviour [8,9]. Hence, this work provides an assessment of finite element (FE) models with Layerwise (LW) descriptions of the displacements – including both linear and high-order kinematics through the discrete layers thickness – aimed for active aeroelastic flutter control analysis of supersonic smart composite panels with surface bonded piezoelectric layers/patches. In addition, to further explore the aeroelastic response of advanced smart composite panels and the role of refined structural models in the intended analyses, it is considered either conventional constant stiffness composite (CSC) laminates with unidirectional fibres or variable stiffness composite (VSC) laminates with curvilinear fibres. Compared to unidirectional fibres counterparts, VSC laminates offer a broader design space of fibres orientations, making them known for their extraordinary tailor-ability in various applications, allowing for buckling enhancement [10], improved vibration response [11], failure resistance optimization [12] and aeroelastic stability augmentation of both wings [13] and supersonic panels [14].

As regards to modelling piezoelectric (constant stiffness) composite panels for active vibration control, Moita el al. [15] applied FE models with Equivalent Single Layer (ESL) descriptions, making use of the Classical Laminated Plate Theory (CLPT) and Reddy's Third-order Shear Deformation Theory (TSDT). In addition, considering active–passive vibration control of smart viscoelastic sandwich panels, Moita et al. [16] adopted a LW model using Reddy's TSDT for the viscoelastic core and the CLPT for the purely elastic and piezoelectric layers. To include the effect of transverse shear deformations beyond the soft viscoelastic core, Araújo et al. [17] considered the First-order Shear Deformation Theory (FSDT) for both elastic composite layers and piezoelectric face layers. Moreira et al. [18] provided an assessment of LW FSDT models with linear and quadratic through-thickness distributions of the electric

* Corresponding author.
E-mail address: joao.anjos.moreira@tecnico.ulisboa.pt (J.A. Moreira).

https://doi.org/10.1016/j.compstruct.2024.118287
Received 16 April 2024; Received in revised form 3 June 2024; Accepted 12 June 2024
Available online 18 June 2024

potential, implemented as user-elements in Abaqus, for static and free vibration analysis of piezoelectric composite plates, including a detailed comparison with three-dimensional (3D) exact solutions by Moleiro et al. [19]. Further refined electro-elastic FE models have been explored making use of the Carrera Unified Formulation (CUF), allowing the accuracy assessment of various kinematic models in a systematic fashion, for the coupled electromechanical static and free vibration analysis of piezoelectric composite plates and shells [20,21]. Moreover, LW mixed least-squares models for static analysis of piezoelectric composite plates are investigated by Moleiro et al. [22], which have been shown to be insensitive to shear locking. Concerning static, free vibration and buckling analysis of purely elastic VSC laminates, there are also some noteworthy works regarding the accuracy assessment of refined LW models [23–29] (most of them derived resorting to CUF). It is worth highlighting that in the design of curvilinear fibre composites, it is crucial to conduct sensitivity analysis of buckling and failure responses to manufacturing defects and fibre misalignments, as discussed by Sánchez-Majano et al. [30] as well as by Pagani and Sánchez-Majano [31,32] resorting to CUF framework. Furthermore, Carrera and Zappino [33] and Zappino et al. [34] applied refined kinematic models within CUF framework for panel flutter analysis of supersonic pinched shells, which are used as thermal insulation panels in launcher structures, though not including any variable stiffness configuration. In the context of flutter analysis of supersonic composite panels with curvilinear fibres, Akhavan and Ribeiro [35] presented a p-version element involving the Vlasov–Reddy TSDT. More recently, Moreira et al. [29] provided a comprehensive assessment of various ESL and LW bi-dimensional type FE models, aimed for the combined flutter and buckling stability analysis of supersonic variable stiffness laminated composites, exploring variable order shear deformation theories (i.e. Taylor z-expansions devoid of thickness stretching) and full Lagrange z-expansions with thickness stretching effects up to the third-order, which is further extended by Moreira et al. [36] for the case of soft core viscoelastic sandwich panels with curvilinear fibre composite skins.

Nonetheless, for aeroelastic flutter analysis and active control of supersonic piezoelectric composite plates, the adopted structural models in the literature tend to be more simple (typically based on ESL descriptions). In addition, the Rayleigh–Ritz method is commonly assumed, in alternative to the FE method, to achieve computationally manageable dynamic systems with reduced dimensions. As a matter of fact, the CLPT stands as the most frequently used axiomatic displacement theory in Rayleigh–Ritz formulations for active panel flutter control analysis [4,5,37–41]. As a result, transverse shear deformations and through-thickness distributions of displacements with zig-zag profile cannot be captured. Even so, some works regarding FE models are also available, considering plate elements with ESL displacement descriptions based on the CLPT [3,42], as well as plate and shell elements with (ESL) FSDT [7,43]. It is worth mentioning that with the exception of the works by Guimarães et al. [40] and Moreira et al. [41], none of the aforementioned papers focuses on the combined application of curvilinear fibre composite laminates and piezoelectric sensors and actuators for aeroelastic control.

In light of the limited number of available literature on the application of LW structural descriptions and high-order kinematic theories for active aeroelastic control analysis, as well as on the combination of curvilinear fibre composites and piezoelectric sensors/actuators, this work provides an assessment variable-order LW shear deformation models for flutter analysis and active aeroelastic control of supersonic smart variable stiffness laminated composite panels. More precisely, the proposed bi-dimensional (2D) type FE models make use of LW displacement descriptions involving three discrete layers, each modelled with either FSDT or TSDT. The aerodynamic loading generated by the supersonic airflow is described by the well-established First-order Piston Theory, as considered in most of the previously mentioned literature regarding supersonic panel flutter. Along with that, the close loop control law is based on feedback proportional gain between the electric potentials of the piezoelectric sensors and actuators, providing active stiffness to the supersonic panel. To the best of the authors' knowledge, this is the first work concerning the evaluation of refined structural models aimed for active aeroelastic flutter control analysis of smart composite panels, exploring piezoelectric composite laminates with either unidirectional or curvilinear fibres, thus making progress on the proper modelling and analysis of advanced smart composites for aerospace applications. Numerical applications are focused on simply supported smart composite panels with either unidirectional or curvilinear fibres, considering various side-to-thickness ratios and control conditions. Whenever thin plates are considered, Rayleigh–Ritz CLPT solutions are also provided in line with Moreira et al. [41]. Therefore, this research allows the accuracy assessment of not only the LW models predictive capabilities but also the simpler and widely used Rayleigh–Ritz formulation with CLPT in active flutter control analysis. Moreover, the aeroelastic flutter response of smart composite panels is investigated, discussing the effect of the proportional control law for both airflow along the x-axis and yawed airflow, as well as for three distinct placement configurations of the piezoelectric patches.

2. Layerwise models

The proposed LW electro-elastic models are developed considering a multilayered composite core with surface bonded piezoelectric layers or patches, taken as a set of three discrete layers – top (t), core (c) and bottom (b), as illustrated in Fig. 1 – under supersonic airflow on the upper surface with in-plane direction Λ and connected to a proportional controller. More specifically, each composite layer can be made of variable stiffness composite with curvilinear fibres having a continuous fibre angle distribution in-plane $\theta(x,y)$, whereas the piezoelectric face layers are considered to be polarized in the thickness direction (i.e. extension mode).

As previously mentioned, the multilayered structural models make use of the FSDT and TSDT at the discrete layer level. Since the number of discrete layers is fixed, the multilayered composite core is then modelled using an ESL description. Hence, the total number of unknown variables is not influenced by the number of actual material/physical layers within the core.

In accordance with linear electroelasticity, the coupled constitutive equations of an orthotropic (transversely poled) piezoelectric layer under plane stress assumptions ($\sigma_{zz} = 0$) are written in the global reference system (x,y,z) as shown:

$$\begin{Bmatrix}\sigma_{xx}\\ \sigma_{yy}\\ \sigma_{yz}\\ \sigma_{xz}\\ \sigma_{xy}\end{Bmatrix} = \begin{bmatrix}\bar{Q}_{11} & \bar{Q}_{12} & 0 & 0 & \bar{Q}_{16}\\ \bar{Q}_{12} & \bar{Q}_{22} & 0 & 0 & \bar{Q}_{26}\\ 0 & 0 & \bar{Q}_{44} & \bar{Q}_{45} & 0\\ 0 & 0 & \bar{Q}_{45} & \bar{Q}_{55} & 0\\ \bar{Q}_{16} & \bar{Q}_{26} & 0 & 0 & \bar{Q}_{66}\end{bmatrix}\begin{Bmatrix}\varepsilon_{xx}\\ \varepsilon_{yy}\\ \gamma_{yz}\\ \gamma_{xz}\\ \gamma_{xy}\end{Bmatrix} - \begin{bmatrix}0 & 0 & \bar{e}_{31}\\ 0 & 0 & \bar{e}_{32}\\ \bar{e}_{14} & \bar{e}_{24} & 0\\ \bar{e}_{15} & \bar{e}_{25} & 0\\ 0 & 0 & \bar{e}_{36}\end{bmatrix}\begin{Bmatrix}E_x\\ E_y\\ E_z\end{Bmatrix} \tag{1a}$$

$$\begin{Bmatrix}D_x\\ D_y\\ D_z\end{Bmatrix} = \begin{bmatrix}0 & 0 & \bar{e}_{14} & \bar{e}_{15} & 0\\ 0 & 0 & \bar{e}_{24} & \bar{e}_{25} & 0\\ \bar{e}_{31} & \bar{e}_{32} & 0 & 0 & \bar{e}_{36}\end{bmatrix}\begin{Bmatrix}\varepsilon_{xx}\\ \varepsilon_{yy}\\ \gamma_{yz}\\ \gamma_{xz}\\ \gamma_{xy}\end{Bmatrix} + \begin{bmatrix}\bar{\epsilon}_{11} & \bar{\epsilon}_{12} & 0\\ \bar{\epsilon}_{12} & \bar{\epsilon}_{22} & 0\\ 0 & 0 & \bar{\epsilon}_{33}\end{bmatrix}\begin{Bmatrix}E_x\\ E_y\\ E_z\end{Bmatrix} \tag{1b}$$

where σ_{ij} represents the stresses, ε_{ii} the infinitesimal normal strains, $\gamma_{ij} = 2\varepsilon_{ij}$ the engineering shear strains, D_i the electric displacement and E_i the electric field. The implied material coefficients are the reduced elastic coefficients $\bar{Q}_{ij}$, reduced piezoelectric coefficients $\bar{e}_{ij}$ and reduced dielectric coefficients $\bar{\epsilon}_{ij}$ [9,44]. For purely elastic materials, such as the fibre reinforced composites considered in this work, the electro-elastic constitutive equations are decoupled since the piezoelectric coefficients are null.

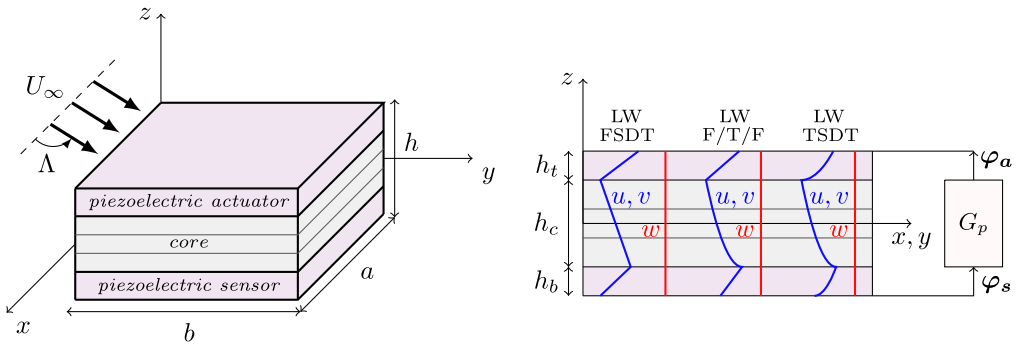

Fig. 1. Illustrative representation of a smart panel with (variable stiffness) laminated composite core along with surface bonded piezoelectric layers, taken as three discrete layers, under supersonic airflow and connected to a proportional controller G_p: geometry and adopted structural theories.

In compact notation, the reduced plane stress electro-elastic constitutive equations of the p-physical layer within the k-sublaminate (discrete layer) are written in the global reference system (x, y, z) as follows:

$$\boldsymbol{\sigma}^{kp} = \bar{\boldsymbol{Q}}^{kp}\boldsymbol{\varepsilon}^{kp} - \bar{\boldsymbol{e}}^{kp}\boldsymbol{E}^{kp} \tag{2a}$$

$$\boldsymbol{D}^{kp} = \bar{\boldsymbol{e}}^{kp^T}\boldsymbol{\varepsilon}^{kp} + \bar{\boldsymbol{\epsilon}}^{kp}\boldsymbol{E}^{kp} \tag{2b}$$

Under the assumption of infinitesimal strains and negligible magnetic effects, the strain–displacements equations and field-potential equations are given by:

$$\varepsilon_{ij} = \frac{1}{2}\left(\frac{\partial u_i}{\partial x_j} + \frac{\partial u_j}{\partial x_i}\right) \tag{3a}$$

$$E_i = -\frac{\partial \phi}{\partial x_i} \tag{3b}$$

where $(u_1, u_2, u_3) \equiv (u, v, w)$ are the displacement components in the x-, y- and z-axis, respectively, such that the displacement vector is $\boldsymbol{u} = \{u\ v\ w\}^T$, whereas ϕ is the electric potential.

The reduced elastic coefficients are obtained by $\bar{\boldsymbol{Q}}^{kp} = \boldsymbol{R}^T(\theta^{kp})\boldsymbol{Q}^{kp}\boldsymbol{R}(\theta^{kp})$ due to the necessary in-plane rotation between the layer material reference system and the global one [9], where the components of the reduced elastic coefficients in the material reference system $\boldsymbol{Q}^{kp}$ as well as the rotation matrix $\boldsymbol{R}(\theta^{kp})$ are given explicitly in [9]. It is worth noting that in curvilinear fibre composite layers, the elastic coefficients in the global reference system are given as in-plane continuous functions, i.e. $\bar{\boldsymbol{Q}}^{kp} = \bar{\boldsymbol{Q}}^{kp}(x, y)$, in line with the fibre angle distribution $\theta^{kp}(x, y)$. In this work, it is considered that each composite layer assumes a linear fibre angle distribution along the x-axis [27,41], as shown:

$$\theta^{kp}(x) = T_0^{kp} + \frac{2(T_1^{kp} - T_0^{kp})}{a}\left|x - \frac{a}{2}\right|, \quad 0 \le x \le a \tag{4}$$

where $T_0^{kp} = \theta^{kp}(a/2)$ and $T_1^{kp} = \theta^{kp}(0) = \theta^{kp}(a)$, as illustrated in Fig. 2.

The LW displacement field is derived making use of the FSDT and TSDT. More precisely, the FSDT and TSDT assume linear and cubic through-thickness distributions of in-plane displacements, taking the form of a Taylor z-expansion around the discrete layer mid-plane, along with a constant distribution of the transverse displacement. To be clear, thickness stretching effects are neglected since its contribution to the supersonic flutter response of thin composite plates (which are the ones of primary interest for aerospace applications) is quite reduced [29], even when considering soft core sandwich panels with high through-thickness inhomogeneity of material properties [36]. Moreover, although it is implied in the well-known Koiter recommendations [45] that a refinement of the transverse shear deformations would call for a simultaneous enrichment of the transverse normal behaviour regarding thickness stretching, it is worth noting that the models based on shear deformation theories devoid of thickness stretching typically have fewer independent variables compared to (quasi-3D) models that include transverse normal deformations.

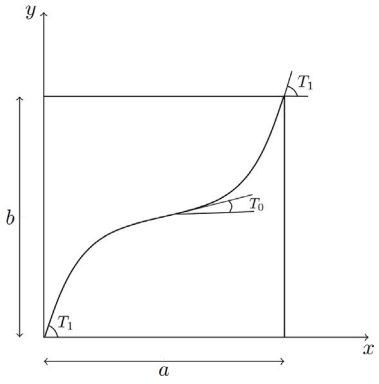

Fig. 2. Variable stiffness composite layer with linear fibre angle distribution along the x-axis.

Imposing the interlaminar continuity of displacements at the interfaces between adjacent layers, the most general case of the displacement field involving the LW TSDT can be derived as shown:

$$u^c(x,y,z) = u_0^c(x,y) + z\theta_x^c(x,y) + z^2\varkappa_x^c(x,y) + z^3\lambda_x^c(x,y) \tag{5a}$$

$$v^c(x,y,z) = v_0^c(x,y) + z\theta_y^c(x,y) + z^2\varkappa_y^c(x,y) + z^3\lambda_y^c(x,y) \tag{5b}$$

$$\begin{aligned} u^t(x,y,z) =& \alpha_1 u_0^c(x,y) + \alpha_2\theta_x^c(x,y) + \alpha_3\varkappa_x^c(x,y) + \alpha_4\lambda_x^c(x,y) + \\ & \left(\alpha_5 + (z - z_0^t)\right)\theta_x^t(x,y) + \left(\alpha_6 + (z - z_0^t)^2\right)\varkappa_x^t(x,y) + \\ & \left(\alpha_7 + (z - z_0^t)^3\right)\lambda_x^t(x,y) \end{aligned} \tag{5c}$$

$$\begin{aligned} v^t(x,y,z) =& \alpha_1 v_0^c(x,y) + \alpha_2\theta_y^c(x,y) + \alpha_3\varkappa_y^c(x,y) + \alpha_4\lambda_y^c(x,y) + \\ & \left(\alpha_5 + (z - z_0^t)\right)\theta_y^t(x,y) + \left(\alpha_6 + (z - z_0^t)^2\right)\varkappa_y^t(x,y) + \\ & \left(\alpha_7 + (z - z_0^t)^3\right)\lambda_y^t(x,y) \end{aligned} \tag{5d}$$

$$\begin{aligned} u^b(x,y,z) =& \beta_1 u_0^c(x,y) + \beta_2\theta_x^c(x,y) + \beta_3\varkappa_x^c(x,y) + \beta_4\lambda_x^c(x,y) + \\ & \left(\beta_5 + (z - z_0^b)\right)\theta_x^b(x,y) + \left(\beta_6 + (z - z_0^b)^2\right)\varkappa_x^b(x,y) + \\ & \left(\beta_7 + (z - z_0^b)^3\right)\lambda_x^b(x,y) \end{aligned} \tag{5e}$$

$$\begin{aligned} v^b(x,y,z) =& \beta_1 v_0^c(x,y) + \beta_2\theta_y^c(x,y) + \beta_3\varkappa_y^c(x,y) + \beta_4\lambda_y^c(x,y) + \\ & \left(\beta_5 + (z - z_0^b)\right)\theta_y^b(x,y) + \left(\beta_6 + (z - z_0^b)^2\right)\varkappa_y^b(x,y) + \\ & \left(\beta_7 + (z - z_0^b)^3\right)\lambda_y^b(x,y) \end{aligned} \tag{5f}$$

$$w^c(x,y,z) = w^t(x,y,z) = w^b(x,y,z) = w_0(x,y) \tag{5g}$$

where u^k, v^k and w^k are the displacements of the k-discrete layer, with $k = \{t, c, b\}$. In addition, the subscript 0 in the displacements identifies the mid-plane location, θ_x^k and θ_y^k stands the rotations of the normals to the mid-plane about the y- and x-axes, respectively, $\varkappa_x^k$, $\varkappa_y^k$, λ_x^k and

λ_y^k are the higher-order generalized displacements of each k-discrete layer. The mid-plane transverse coordinates are $z_0^t = (h_t + h_c)/2$ and $z_0^b = -(h_b + h_c)/2$. Moreover, the variables α_n and β_n are derived from the interlaminar continuity conditions as follows:

$$\alpha_1 = 1,\ \alpha_2 = h_c/2,\ \alpha_3 = \alpha_2^2,\ \alpha_4 = \alpha_2^3,\ \alpha_5 = h_t/2,\ \alpha_6 = -\alpha_5^2,\ \alpha_7 = \alpha_5^3 \quad (6a)$$

$$\beta_1 = 1,\ \beta_2 = -h_c/2,\ \beta_3 = \beta_2^2,\ \beta_4 = -\beta_2^3,\ \beta_5 = -h_b/2,\ \beta_6 = -\beta_5^2,\ \beta_7 = \beta_5^3 \quad (6b)$$

Since the FSDT can be derived as a particular case of the TSDT, the LW TSDT displacement field presented in Eq. (5) includes implicitly other simpler kinematic descriptions, which can be recovered when neglecting some specific terms. On one hand, the LW model making use of the FSDT for the top and bottom discrete layers and the TSDT for the core (denoted as LW F/T/F) is obtained by neglecting the high-order terms associated to $k = t$ and b in Eqs. (5c) to (5f). On the other hand, the piecewise FSDT model is recovered by neglecting all high-order generalized displacements. Specifically, the twenty one degrees of freedom (DOFs) associated to the LW TSDT model are $\boldsymbol{d} = \{u_0^c\ v_0^c\ w_0^c\ \theta_x^c\ \theta_y^c\ \varkappa_x^c\ \varkappa_y^c\ \lambda_x^c\ \lambda_y^c\ \theta_x^t\ \theta_y^t\ \varkappa_x^t\ \varkappa_y^t\ \lambda_x^t\ \lambda_y^t\ \theta_x^b\ \theta_y^b\ \varkappa_x^b\ \varkappa_y^b\ \lambda_x^b\ \lambda_y^b\}^T$, whereas for the LW F/T/F model, only thirteen DOFs remain since the high-order terms of the top and bottom layers are neglected. For the LW FSDT model, no high-order generalized displacement is included and therefore only nine DOFs remain.

In view of the constant through-thickness distribution of shear strains predicted by the FSDT, a shear correction factor K_s is commonly applied for the evaluation of transverse shear stresses in first-order models [9]. This is avoided altogether by the more refined TSDT. In the present work, no shear corrections factor is introduced in the LW FSDT and LW F/T/F models, i.e. $K_s = 1$, as followed by Moreira et al. [18,27,29].

Assuming that the electric potential has a linear through-thickness distribution [18,41] such that it is applied to piezoelectric layers resorting to surface electrodes, the in-plane electric field components are null ($E_x = E_y = 0$) and the constant transverse electric field can be written as shown:

$$E_z^k = -\frac{\Delta\phi^k}{h^k} \quad (7)$$

where $\Delta\phi^k$ represents the electric potential difference between the upper and lower surfaces of the piezoelectric layer (noting that $\Delta\phi^k = 0$ for purely elastic layers).

3. FE formulation

The Principle of Hamilton is applied to derive the dynamic electro-elastic equilibrium equations of the piezoelectric composite panel under supersonic airflow on its upper surface ($z = h/2$), assuming that the resulting aerodynamic pressure Δp is described by the First-order Piston Theory. Hence, considering the piezoelectric composite panel taken as k discrete layers with in-plane surface S and thickness domain h^k, the variational formulation comes out as shown:

$$\sum_k \int_S \int_{h^k} \delta\boldsymbol{\varepsilon}^{k^T}\boldsymbol{\sigma}^k - \delta\boldsymbol{E}^{k^T}\boldsymbol{D}^k + \rho^k\delta\boldsymbol{u}^{k^T}\ddot{\boldsymbol{u}}^k\ dz dS = \int_S \delta\boldsymbol{u}^{t^T}|_{\frac{h}{2}}\boldsymbol{e}_z\Delta p\ dS + \int_{S_f}\delta\boldsymbol{u}^{k^T}|_{z_{S_f}}\boldsymbol{f}\ dS \quad (8)$$

where δ stands for the variational operator, the double-dot denotes the second time derivative, ρ^k is the k-layer density and $\boldsymbol{e}_z = \{0\ 0\ 1\}^T$. In addition to the aerodynamic loading, an external mechanical load $\boldsymbol{f} = \{q_x\ q_y\ q_z\}^T$ is also considered to be applied on the surface S_f located at the transverse coordinate z_{S_f}.

The aerodynamic loading is described using the well-known First-order Piston Theory, which is a simple and widely used aerodynamic model in the context of supersonic panel flutter, providing accurate results in the high supersonic range [33,46,47]. In agreement with the First-order Piston Theory, the transverse loading resulting from the pressure difference generated by the supersonic airflow with yaw angle Λ is given by:

$$\Delta p = -\lambda\left(\frac{\partial w}{\partial x}\cos\Lambda + \frac{\partial w}{\partial y}\sin\Lambda\right) - g_a\frac{\partial w}{\partial t} \quad (9)$$

such that the dynamic pressure parameter λ and aerodynamic damping g_a are written as:

$$\lambda = \frac{\rho_\infty U_\infty^2}{\beta} \quad (10a)$$

$$g_a = \frac{\lambda}{U_\infty}\frac{(M_\infty^2 - 2)}{(M_\infty^2 - 1)} \quad (10b)$$

where ρ_∞, U_∞ and M_∞ denote the density, speed and Mach number of the free airflow and $\beta = \sqrt{M_\infty^2 - 1}$. For $M_\infty \gg 1$, it is commonly assumed that $\mu[(M_\infty^2 - 2)/(M_\infty^2 - 1)]^2/\beta \approx \mu/M_\infty$ [5,48], where $\mu = \rho_\infty a/(\rho h)$ denotes the mass ratio, and therefore the aerodynamic damping can be approximated by:

$$g_a = \sqrt{\frac{\rho h}{a}}\sqrt{\lambda\frac{\mu}{M_\infty}} \quad (11)$$

In engineering practice, the ratio μ/M_∞ typically ranges between 0.01 and 0.1 for aerospace structures [46–48]. Actually, the aerodynamic damping has a stabilizing effect in the occurrence of flutter and leads to slightly higher flutter bounds, as carefully demonstrated in the numerical applications. Hence, more conservative flutter analyses can be ensured, from a design standpoint, by imposing $g_a = 0$ in Eq. (9), as also followed in [14,41], which corresponds to assuming $\mu/M_\infty = 0$ in Eq. (11).

As regards to the FE approximation, it is presented making use of a general notation in matrix form, where the dimensions and components of the matrices are dependent on the adopted kinematic theory. Hence, for an arbitrary k-discrete layer, the 1D z-expansions and 2D FE approximations of $\boldsymbol{u}^k$ and $\boldsymbol{\varepsilon}^k$ are defined as follows:

$$\boldsymbol{u}^k = \boldsymbol{Z}^k\boldsymbol{N}^k\boldsymbol{d} \quad (12a)$$

$$\boldsymbol{\varepsilon}^k = \boldsymbol{S}^k\boldsymbol{B}^k\boldsymbol{d} \quad (12b)$$

where $\boldsymbol{Z}^k$ and $\boldsymbol{S}^k$ contain the z-expansion functions and their derivatives through the discrete layer thickness, while $\boldsymbol{N}^k$ and $\boldsymbol{B}^k$ define the necessary FE approximations in-plane using 2D shape functions. The adopted 2D shape functions are quadratic Lagrange functions, corresponding to the standard nine-node quadrilateral element [9] (Q9), such that the element DOFs are structured as $\boldsymbol{d} = \{\boldsymbol{d}_1^T\ \ldots\ \boldsymbol{d}_9^T\}^T$, where $\boldsymbol{d}_i$ stands for the nodal DOFs. The C^0-interpolation in-plane, required by the adopted structural FE models, is then fulfilled by the 2D Lagrange polynomials, thus ensuring the interelement continuity of primary variables (as in a conforming element).

When considering multiple piezoelectric patches, the electric potential vector for $k = \{t, b\}$ is written as $\boldsymbol{\varphi}^k = \{\Delta\phi^{k1}\ \ldots\ \Delta\phi^{kNPP}\}^T$, where NPP stands for the number of piezoelectric patches in each side of the panel. Since the piezoelectric layers are covered with surface electrodes, which means equipotential conditions in-plane, the total number of electrical DOFs is $2\times NPP$. In line with Eq. (7), the electric field vector is defined as shown:

$$\boldsymbol{E}^k = -\boldsymbol{S}_\phi^k\boldsymbol{B}_\phi^k\boldsymbol{\varphi}^k \quad (13)$$

such that the matrices $\boldsymbol{S}_\phi^k$ and $\boldsymbol{B}_\phi^k$ are given by:

$$\boldsymbol{S}_\phi^k = \left[(\boldsymbol{e}_z)_1\ \ldots\ (\boldsymbol{e}_z)_{NPP}\right] \quad (14a)$$

$$\boldsymbol{B}_\phi^k = \left(1/h^k\right)\boldsymbol{\mathcal{I}} \quad (14b)$$

where $\boldsymbol{\mathcal{I}}$ represents the identity tensor with dimension $NPP\times NPP$. Note that for each side of the panel, the patches have the same thickness – either h^t or h^b, depending on the side of the panel – and are assumed to be equally distributed in the upper and lower surfaces of the composite core.

Introducing the approximations given in Eqs. (12) and (13), the constitutive relations in Eqs. (2) as well as the aerodynamic pressure distribution in Eq. (9), all together, into Eq. (8), gives rise to the element equilibrium equations. The aero-electro-elastic equilibrium equations of the element can then be written separating the electrical DOFs of the top and bottom layers as follows:

$$\boldsymbol{M}_{uu}\ddot{\boldsymbol{d}} + g_a\boldsymbol{C}_{\Delta p}\dot{\boldsymbol{d}} + (\boldsymbol{K}_{uu} + \lambda\boldsymbol{K}_{\Delta p})\boldsymbol{d} + \boldsymbol{K}^t_{u\phi}\boldsymbol{\varphi}^t + \boldsymbol{K}^b_{u\phi}\boldsymbol{\varphi}^b = \boldsymbol{F}_u \tag{15a}$$

$$\boldsymbol{K}^{t^T}_{u\phi}\boldsymbol{d} + \boldsymbol{K}^t_{\phi\phi}\boldsymbol{\varphi}^t = \boldsymbol{0} \tag{15b}$$

$$\boldsymbol{K}^{b^T}_{u\phi}\boldsymbol{d} + \boldsymbol{K}^b_{\phi\phi}\boldsymbol{\varphi}^b = \boldsymbol{0} \tag{15c}$$

where $\boldsymbol{M}_{uu}$, $g_a\boldsymbol{C}_{\Delta p}$, $\boldsymbol{K}_{uu}$, $\lambda\boldsymbol{K}_{\Delta p}$, $\boldsymbol{K}^k_{u\phi}$ and $\boldsymbol{K}^k_{\phi\phi}$ are the mass, aerodynamic damping, purely elastic stiffness, aerodynamic stiffness, electromechanical coupling stiffness and dielectric stiffness matrices of the element, respectively, while $\boldsymbol{F}_u$ is the element mechanical load vector.

As derived from the variational formulation and taking into account that, in the most general case, each k-discrete layer can represent a sublaminate with N^k_p physical layers, the implied element matrices come out as shown:

$$\boldsymbol{M}_{uu} = \sum_{k=t,c,b}\sum_{p=1}^{N^k_p}\int_{\Omega}\boldsymbol{N}^{k^T}\left(\int_{h^{kp}}\rho^{kp}\boldsymbol{Z}^{k^T}\boldsymbol{Z}^k dz\right)\boldsymbol{N}^k d\Omega \tag{16a}$$

$$\boldsymbol{K}_{uu} = \sum_{k=t,c,b}\sum_{p=1}^{N^k_p}\int_{\Omega}\boldsymbol{B}^{k^T}\left(\int_{h^{kp}}\boldsymbol{S}^{k^T}\bar{\boldsymbol{Q}}^{kp}\boldsymbol{S}^k dz\right)\boldsymbol{B}^k d\Omega \tag{16b}$$

$$\boldsymbol{K}^k_{u\phi} = \sum_{p=1}^{N^k_p}\int_{\Omega}\boldsymbol{B}^{k^T}\left(\int_{h^{kp}}\boldsymbol{S}^{k^T}\bar{\boldsymbol{e}}^{kp}\boldsymbol{S}^k_{\phi} dz\right)\boldsymbol{B}^k_{\phi} d\Omega \tag{16c}$$

$$\boldsymbol{K}^k_{\phi\phi} = \sum_{p=1}^{N^k_p}\int_{\Omega}\boldsymbol{B}^{k^T}_{\phi}\left(\int_{h^{kp}}\boldsymbol{S}^{k^T}_{\phi}\bar{\boldsymbol{\epsilon}}^{kp}\boldsymbol{S}^k_{\phi} dz\right)\boldsymbol{B}^k_{\phi} d\Omega \tag{16d}$$

$$\boldsymbol{C}_{\Delta p} = \int_{\Omega}\boldsymbol{N}^{t^T}\boldsymbol{Z}^{t^T}|_{\frac{h}{2}}\boldsymbol{e}_z\boldsymbol{e}_z^T\boldsymbol{Z}^t|_{\frac{h}{2}}\boldsymbol{N}^t d\Omega \tag{16e}$$

$$\boldsymbol{K}_{\Delta p} = \int_{\Omega}\boldsymbol{N}^{t^T}\boldsymbol{Z}^{t^T}|_{\frac{h}{2}}\boldsymbol{e}_z\boldsymbol{e}_z^T\boldsymbol{Z}^t|_{\frac{h}{2}}\left(\frac{\partial\boldsymbol{N}^t}{\partial x}\cos\Lambda + \frac{\partial\boldsymbol{N}^t}{\partial y}\sin\Lambda\right)d\Omega \tag{16f}$$

$$\boldsymbol{F}_u = \sum_{k=t,c,b}\int_{\Omega}\boldsymbol{N}^{k^T}\boldsymbol{Z}^{k^T}|_{z_{S_f}}\boldsymbol{f}^k d\Omega \tag{16g}$$

It is worth remarking that the 1D integrals in each thickness domain h^{kp} are evaluated using exact integration, whereas the integration in the in-plane FE domain Ω is performed numerically, making use of Gauss quadrature, considering reduced integration for the shear terms of the stiffness purely elastic matrix (Eq. (16b)) to avoid shear locking effects [9]. Additionally, when considering variable stiffness composite layers with curvilinear fibres, the fibre angle is evaluated at the location of each integration point to ensure the most accurate prediction of the elastic coefficients.

4. Aeroelastic equilibrium equations with active control

As illustrated in Fig. 1, the top piezoelectric layer is taken as the actuator layer (a), whereas the bottom layer is the sensor layer (s). In view of the adopted nomenclature in Eq. (15), it is thus equivalent to consider $a \equiv t$ and $s \equiv b$. Therefore, after the standard FE assemblage and imposition of boundary conditions, one obtains the global system of equilibrium equations as shown:

$$\begin{bmatrix}\boldsymbol{M}_{uu} & \boldsymbol{0} & \boldsymbol{0}\\ \boldsymbol{0} & \boldsymbol{0} & \boldsymbol{0}\\ \boldsymbol{0} & \boldsymbol{0} & \boldsymbol{0}\end{bmatrix}\begin{Bmatrix}\ddot{\boldsymbol{\Delta}}\\ \ddot{\boldsymbol{\varphi}}^s\\ \ddot{\boldsymbol{\varphi}}^a\end{Bmatrix} + \begin{bmatrix}g_a\boldsymbol{C}_{\Delta p} & \boldsymbol{0} & \boldsymbol{0}\\ \boldsymbol{0} & \boldsymbol{0} & \boldsymbol{0}\\ \boldsymbol{0} & \boldsymbol{0} & \boldsymbol{0}\end{bmatrix}\begin{Bmatrix}\dot{\boldsymbol{\Delta}}\\ \dot{\boldsymbol{\varphi}}^s\\ \dot{\boldsymbol{\varphi}}^a\end{Bmatrix}$$
$$+ \begin{bmatrix}\boldsymbol{K}_{uu} + \lambda\boldsymbol{K}_{\Delta p} & \boldsymbol{K}^s_{u\phi} & \boldsymbol{K}^a_{u\phi}\\ \boldsymbol{K}^{s^T}_{u\phi} & \boldsymbol{K}^s_{\phi\phi} & \boldsymbol{0}\\ \boldsymbol{K}^{a^T}_{u\phi} & \boldsymbol{0} & \boldsymbol{K}^a_{\phi\phi}\end{bmatrix}\begin{Bmatrix}\boldsymbol{\Delta}\\ \boldsymbol{\varphi}^s\\ \boldsymbol{\varphi}^a\end{Bmatrix} = \begin{Bmatrix}\boldsymbol{F}_u\\ \boldsymbol{0}\\ \boldsymbol{0}\end{Bmatrix} \tag{17}$$

where $\boldsymbol{\Delta}$, $\dot{\boldsymbol{\Delta}}$ and $\ddot{\boldsymbol{\Delta}}$ are the mechanical DOFs and corresponding time derivatives.

From the equation associated to the electrical DOFs of the sensors, the generated electric potential is obtained by:

$$\boldsymbol{\varphi}^s = -\boldsymbol{K}^{s^{-1}}_{\phi\phi}\boldsymbol{K}^{s^T}_{u\phi}\boldsymbol{\Delta} \tag{18}$$

Assuming now that the piezoelectric layers are connected to a proportional controller, with feedback control gain G_p, the electric potential of the actuators is governed by the following control law:

$$\boldsymbol{\varphi}^a = G_p\boldsymbol{\varphi}^s = -G_p\boldsymbol{K}^{s^{-1}}_{\phi\phi}\boldsymbol{K}^{s^T}_{u\phi}\boldsymbol{\Delta} \tag{19}$$

Introducing Eqs. (18) and (19) into the equation associated with the mechanical DOFs in Eq. (17), the final aeroelastic equilibrium is written as follows:

$$\boldsymbol{M}_{uu}\ddot{\boldsymbol{\Delta}} + g_a\boldsymbol{C}_{\Delta p}\dot{\boldsymbol{\Delta}} + (\boldsymbol{K}^* + \lambda\boldsymbol{K}_{\Delta p})\boldsymbol{\Delta} = \boldsymbol{F}_u(t) \tag{20}$$

where the condensed stiffness matrix $\boldsymbol{K}^*$ comes out as shown:

$$\boldsymbol{K}^* = \boldsymbol{K}_{uu} - (G_p\boldsymbol{K}^a_{u\phi} + \boldsymbol{K}^s_{u\phi})\boldsymbol{K}^{s^{-1}}_{\phi\phi}\boldsymbol{K}^{s^T}_{u\phi} \tag{21}$$

In the absence of applied mechanical loads and assuming harmonic solutions in the form of $\boldsymbol{\Delta} = \hat{\boldsymbol{\Delta}}e^{s_n t}$, the characteristic equation of the global (quadractic) eigenvalue problem can be written as follows:

$$\left|s_n^2\boldsymbol{M}_{uu} + s_n g_a\boldsymbol{C}_{\Delta p} + \boldsymbol{K}^* + \lambda\boldsymbol{K}_{\Delta p}\right| = 0 \tag{22}$$

where the complex eigenvalue of the n-mode is represented by $s_n^2 = -\omega_n^2(1 + ig_n)$, with $i = \sqrt{-1}$. Hence, for a given flow condition defined through the dynamic pressure parameter λ, which also defines the aerodynamic damping parameter g_a through Eq. (11), the solution of the eigenvalue problem yields the natural frequencies (ω_n) and modal loss factors (g_n). The particular case of free vibration in vacuum is obtained by setting $\lambda = 0$ and $g_a = 0$ in Eq. (22). In addition, for Short Circuit (SC) conditions of the surface electrodes ($\boldsymbol{\varphi}^s = \boldsymbol{\varphi}^a = 0$), one has $\boldsymbol{K}^* = \boldsymbol{K}_{uu}$. In this work, the SC conditions will be representative of an uncontrolled system, whereas for any non zero control gain G_p, the active control system is considered to be operational.

In aeroelastic flutter analysis, the aim is to determine the lowest dynamic pressure parameter, known as critical flutter pressure parameter λ_F, for which the system becomes dynamically unstable, i.e. with at least one negative modal loss factor ($g_n < 0$). In the absence of aerodynamic and structural damping, the flutter bound is also characterized by the appearance of modes with complex conjugated pairs of eigenvalues, which leads to the coalescence of natural frequencies of the modes involved in flutter. Moreover, when neglecting the aerodynamic damping in Eq. (22), the characteristic equation of the (linear) eigenvalue problem takes the standard form, as shown:

$$\left|s_n^2\boldsymbol{M}_{uu} + \boldsymbol{K}^* + \lambda\boldsymbol{K}_{\Delta p}\right| = 0 \tag{23}$$

For any initial perturbation (e.g. an applied transverse load or displacement), the aeroelastic response can also be obtained in the time domain, making use of the well-known Newmark method, for instance, to solve Eq. (20). In fact, the Newmark method will be applied later on to obtain the time response of supersonic smart panels which are initially subjected to an applied (single-peak) bi-sinusoidal transverse load in the form of $q_z(x, y) = q_0\sin(\pi x/a)\sin(\pi y/b)$.

5. Numerical applications

The proposed LW models predictive capabilities are now assessed and compared through selected numerical applications, which are divided into three parts. Section 5.1 is focused on the convergence analysis of both free vibration and supersonic flutter solutions, and includes a preliminary evaluation of the impact of the proportional control gain and aerodynamic damping on the aeroelastic response. Section 5.2. is dedicated to the aeroelastic flutter analysis of simply supported smart panels with laminated composite core, using either

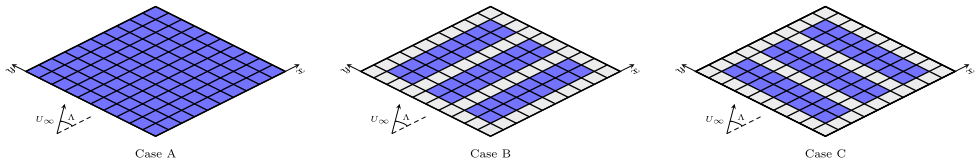

Fig. 3. Different placement configurations of the piezoelectric patches in the smart composite panels ($z = \pm h/2$ and 10 × 10 Q9).

unidirectional or curvilinear fibres, and surface bonded piezoelectric layers. In addition to thin panels, which are of primary interest for most aerospace applications, moderately thick panels are also investigated to trigger more complicated effects that may occur, relying mostly on high-order kinematic refinements to be properly captured. The aeroelastic response behaviour of supersonic smart panels with active proportional control is demonstrated and discussed, regarding the influence of some design parameters, such as the control gain and the airflow direction. Section 5.3. is concerned with the comparison of three distinct placement configurations of piezoelectric sensors and actuators on the aeroelastic flutter stability of thin panels.

For numerical applications purposes, the intended multilayered panels are square plates with fixed in-plane dimensions $a = b = 1$ m and a total thickness h varied to consider different side-to-thickness ratios, namely, $a/h = 250$, 100, 50 and 25, i.e. from thin to moderately thick plates, respectively. The assumed core thickness ratio is $h_c/h = 0.9$, leaving each piezoelectric layer with $0.05h$ of thickness. In fact, the laminated core consists of three equal thickness composite layers, according to the following stacking sequences:

- *Smart CSC cross-ply laminate*: (PZT-4/0/90/0/PZT-4);
- *Smart VSC1 laminate*: (PZT-4/⟨0, 45⟩/⟨-45, -60⟩/⟨0, 45⟩/PZT-4);
- *Smart VSC2 laminate*: (PZT-4/⟨30, 0⟩/⟨45, 90⟩/⟨30, 0⟩/PZT-4).

where $\langle T_0^{kp}, T_1^{kp} \rangle$ stands for the pair of control angles defined in the linear fibre angle variation given in Eq. (4). The stacking sequences of the composite core are based on previous works by the authors [27,41], thus extending the available benchmark solutions concerning static, free vibration and flutter behaviour to the case of active aeroelastic control.

The material properties of the piezoelectric layers, as a transversely isotropic and thickness poled PZT-4, are $E_1 = E_2 = 81.3$ GPa, $E_3 = 64.5$ GPa, $G_{12} = 30.6$ GPa, $G_{13} = G_{23} = 25.6$ GPa, $\nu_{12} = 0.329$, $\nu_{13} = \nu_{23} = 0.432$, $e_{31} = e_{32} = -5.20$ C/m^2, $e_{33} = 15.08$ C/m^2, $e_{15} = e_{24} = 12.72$ C/m^2, $\epsilon_{11} = \epsilon_{22} = 1475\epsilon_0$, $\epsilon_{33} = 1300\epsilon_0$ ($\epsilon_0 = 8.85 \times 10^{-12}$ F/m) and $\rho = 7500$ kg/m^3, whereas the material properties of the core layers, as an (orthotropic) graphite-epoxy fibre reinforced composite, are $E_1 = 25E_0$, $E_2 = E_3 = E_0$, $G_{12} = G_{13} = 0.5E_0$, $G_{23} = 0.2E_0$, $\nu_{12} = \nu_{13} = \nu_{23} = 0.25$ and $\rho = 1600$ kg/m^3, where $E_0 = 7$ GPa.

Regarding the placement configurations of the piezoelectric sensors and actuators, three distinct cases are examined, which are denoted as Case A, B and C, in agreement with Fig. 3. Specifically, in Case A, a fully covered panel is investigated, whereas in Cases B and C it is considered six strips of patches (three strips on each side of the panel), with each patch strip of in-plane dimensions $0.8a$×$0.2b$ and $0.2a$×$0.8b$, respectively. As illustrated in Fig. 3, in Case B, the patch strips are aligned along the x-axis, while in Case C, the patch strips are aligned along the y-axis.

For most numerical applications, the airflow is considered along the x-axis (i.e., yaw angle $\Lambda = 0°$). However, for comparison purposes, the investigation of yawed airflow with $\Lambda = 45°$ is also carried out in the case of thin plates fully covered by piezoelectric layers (Case A), with $a/h = 250$. The flutter dynamic pressure parameters λ_F are given in the following nondimensionalized form:

$$\tilde{\lambda}_F = \frac{\lambda_F a^3}{h^3 G_{12}^c} \tag{24}$$

where G_{12}^c stands for the shear modulus G_{12} of the composite material.

To be clear, the simply supported boundary conditions imposed, at the layer level, are as follows:

$$u^k = w^k = 0 \text{ at } y = 0, b \tag{25a}$$

$$v^k = w^k = 0 \text{ at } x = 0, a \tag{25b}$$

Additionally, the intended assessment of LW models in aeroelastic flutter analysis of thin smart composite panels fully covered by piezoelectric layers (Case A, Fig. 3) is performed by a comparison with Rayleigh–Ritz solutions, as developed by Moreira et al. [41]. In more detail, the Rayleigh–Ritz formulation adopted in [41] is based on an ESL structural model involving the CLPT and, therefore, transverse shear deformations are neglected (as opposed to the proposed LW FE models which include discrete layer shear deformation effects). The Rayleigh–Ritz CLPT solutions (denoted by RR CLPT) are provided in the interest of the present work, thus made available for the first-time. It is worth remarking that for the smart cross-ply composite laminate, the Rayleigh–Ritz approximation is defined resorting to trigonometric expansion functions, whereas for the smart VSC laminates, it is considered Legendre polynomials as expansion functions. In fact, the application of trigonometric expansions for the analysis of highly anisotropic laminates involving bending–twisting coupling, such as any composite with curvilinear fibres, leads to an overestimation of the bending stiffness, as shown in [29,41]. On the other hand, Legendre polynomials have been proven accurate for the modelling of composite laminates with curvilinear fibres [40,49]. Since only bending deformations are retained in the formulation adopted in Moreira et al. [41], along with sinusoidal expansion functions, further insights are given in Appendix with respect to the RR CLPT model including membrane deformations as well as in-plane expansions making use of Legendre polynomials.

5.1. Convergence analysis

In Table 1, the convergence analysis results of the LW FSDT model are provided, considering both free vibration in vacuum and flutter analysis of the smart *VSC1* laminate with $a/h = 250$ under airflow aligned with the x-axis, i.e. $\Lambda = 0°$. In particular, the first eight natural frequencies are considered in free vibration analysis, whereas in flutter analysis it is presented the nondimensionalized flutter dynamic pressure parameter $\tilde{\lambda}_F$ and the corresponding flutter frequency f_F (which is defined as the value for which the natural frequencies of the modes involved in flutter coalesce at the flutter bound). The FE solutions are provided alongside RR CLPT solutions, considering either only bending deformations or both membrane and bending deformations. The RR CLPT solutions are obtained with ten terms in each in-plane direction, making use of Legendre polynomials as expansion functions (thus ensuring converged solutions). Moreover, the aerodynamic damping is neglected in the flutter solutions presented in Table 1.

Comparing the numerical results presented in Table 1, it is concluded that the first eight natural frequencies and the flutter parameters start to converge for meshes with more than 10 × 10 Q9 elements, regardless of the applied control gain. The present RR CLPT solutions with both bending and membrane deformations involve a total of 300 mechanical DOFs, whereas the LW FSDT, LW F/T/F and LW TSDT models with 10 × 10 Q9 elements lead to 3969, 5733 and 9261 mechanical DOFs, respectively. Hence, the computation of the eigenvalues is three to five times faster when considering the RR model, especially as compared to the most refined model (LW TSDT). Nonetheless, each

Table 1
Convergence analysis results of the LW FSDT model: first eight natural frequencies f_n (Hz), nondimensionalized flutter pressure parameter $\tilde{\lambda}_F$ and flutter frequency f_F (Hz) of the (PZT-4/⟨0, 45⟩/⟨-45, -60⟩/⟨0, 45⟩/PZT-4) smart *VSC1* laminated panel ($a/h = 250$, $\Lambda = 0°$) under short circuit (SC) conditions or active proportional control G_p.

	Mesh	f_1	f_2	f_3	f_4	f_5	f_6	f_7	f_8	$\tilde{\lambda}_F$	f_F
SC	6 × 6	21.24	42.14	59.51	75.60	82.85	114.30	124.26	130.52	996.2	45.42
	8 × 8	21.23	42.08	59.39	75.24	82.52	113.59	123.26	128.15	996.7	45.47
	10 × 10	21.22	42.06	59.35	75.14	82.42	113.38	122.96	127.45	996.8	45.48
	12 × 12	21.22	42.05	59.33	75.10	82.38	113.30	122.85	127.20	996.8	45.48
	RR CLPT[a]	21.23	42.08	59.40	75.18	82.50	113.52	123.10	127.26	998.4	45.50
	RR CLPT	21.23	42.08	59.40	75.18	82.50	113.52	123.10	127.26	998.4	45.50
$G_p = 5$	6 × 6	20.44	42.14	59.51	75.17	82.73	114.30	123.79	130.52	1052.2	46.39
	8 × 8	20.43	42.08	59.39	74.81	82.41	113.59	122.81	128.15	1053.5	46.46
	10 × 10	20.42	42.06	59.35	74.71	82.31	113.38	122.52	127.45	1053.8	46.48
	12 × 12	20.41	42.05	59.33	74.67	82.26	113.30	122.41	127.20	1053.9	46.49
	RR CLPT[a]	20.33	42.08	59.40	74.70	82.38	113.52	122.61	127.26	1062.4	46.63
	RR CLPT	20.42	42.08	59.40	74.75	82.39	113.52	122.66	127.26	1055.6	46.50
$G_p = 20$	6 × 6	17.29	42.14	59.51	73.60	82.39	114.30	122.32	130.52	1350.0	53.13
	8 × 8	17.27	42.08	59.39	73.25	82.10	113.59	121.38	128.15	1359.7	53.51
	10 × 10	17.25	42.06	59.35	73.15	82.00	113.38	121.10	127.45	1362.5	53.61
	12 × 12	17.24	42.05	59.33	73.12	81.96	113.30	120.99	127.20	1363.5	53.65
	RR CLPT[a]	14.83	42.08	59.40	72.21	81.95	113.52	120.44	127.26	1410.0	67.16
	RR CLPT	17.24	42.08	59.40	73.19	82.09	113.52	121.23	127.26	1365.8	53.67

[a] Only bending deformations retained.

eigenvalue solution is obtained within a maximum of just a couple of seconds using the Matlab environment on a computer with an Apple M2 Pro chip, 32 GB of memory, and macOS 13.2.1 (22D68). In fact, the main advantage of the RR CLPT model lies in its low computational cost, making it particularly useful for preliminary analysis and design. Moreover, the use of 10 × 10 Q9 elements does not increase significantly the computational time as compared to the more coarse meshes with 8 × 8 or 6 × 6 Q9 elements (between 15% to 30%, depending on the LW model). As a result, the mesh with 10 × 10 Q9 elements is applied for the following flutter analyses, ensuring the necessary numerical accuracy, while maintaining fast and computationally efficient flutter predictions. Even though not shown, for brevity, it is worth mentioning that: (i) a similar convergence behaviour is obtained when considering the remaining kinematic models; and (ii) the convergence of the mode shapes is also ensured, as necessary, considering either free vibrations in vacuum or under the effect of supersonic airflow. By adopting the same FE mesh for all LW models, the accuracy assessment is focused on the refinements introduced in the z-expansions of the in-plane displacements, as intended by this work.

It is also relevant to mention that both RR CLPT (including membrane deformations) and LW FSDT (FE) solutions estimate the occurrence of flutter due to the first two modes for either SC conditions or active control conditions. Comparing the RR CLPT and FE solutions, it is observed that the free vibration and flutter results are in good agreement for SC conditions and active control with $G_p = 5$. However, for the higher gain, $G_p = 20$, the RR CLPT model devoid of membrane deformations underpredicts the fundamental frequency by 16% and overpredicts the flutter pressure parameter and flutter frequency by 4% and 25%, respectively (since it is estimated that in the absence of membrane deformations, flutter occurs due to high-order modes, namely the third and fourth modes). Nonetheless, the RR CLPT solutions with both membrane and bending deformations are in line with the FE solutions, regardless of the applied control gain (maximum discrepancy of 0.2% regarding the flutter pressure parameter, which occurs for $G_p = 20$).

In more detail, when considering SC conditions, the inclusion of the membrane deformations in the RR CLPT model does not affect the free vibration and flutter solutions. In contrast, as the control gain increases, the membrane deformations and membrane stress resultants induced by the applied electric potential play a more pronounced role in the mechanical response behaviour. Even though the comparison of RR CLPT and FE solutions is further discussed in the following subsection, it is relevant to emphasize, at this point, that the membrane deformations are indeed mandatory to ensure accurate free vibration and flutter solutions in smart laminates with active proportional control for any value of control gain. Therefore, in ensuing assessments making use of the RR CLPT based model, both membrane and bending deformations are taken into account.

Table 2
Nondimensionalized flutter dynamic pressure parameters $\tilde{\lambda}_F$ and flutter frequencies f_F (Hz) of the (PZT-4/⟨0, 45⟩/⟨-45, -60⟩/⟨0, 45⟩/PZT-4) smart *VSC1* laminated panel ($a/h = 250$, $\Lambda = 0°$), including aerodynamic damping (results obtained using the LW FSDT model and 10 × 10 Q9 elements).

	$\mu/M_\infty = 0$		$\mu/M_\infty = 0.01$		$\mu/M_\infty = 0.1$	
	$\tilde{\lambda}_F$	f_F	$\tilde{\lambda}_F$	f_F	$\tilde{\lambda}_F$	f_F
SC	996.8	45.48	1003.5	45.64	1061.7	47.04
$G_p = -5$	921.0	44.29	927.3	44.43	983.0	45.71
$G_p = -20$	764.0	42.33	769.6	42.44	820.6	43.49
$G_p = 5$	1053.8	46.48	1060.9	46.65	1120.7	48.14
$G_p = 20$	1362.5	53.61	1369.8	53.80	1428.2	55.08

Before moving on into the models comparison, *per se*, the inclusion of the aerodynamic damping is investigated in Table 2, assuming airflow along the x-axis. In agreement with Eq. (11), the aerodynamic damping parameter is estimated for two values of the ratio μ/M_∞, namely 0.01 and 0.1. The solutions without aerodynamic damping (denoted by $\mu/M_\infty = 0$) are also included in Table 2 for comparison purposes. Furthermore, to examine the effect of the proportional control gain sign, the numerical results include the case of SC conditions (uncontrolled configuration) as well as the cases of $G_p = \pm 5$ and $G_p = \pm 20$ (controlled configurations).

Table 2 reveals that the aerodynamic damping has a stabilizing effect on the occurrence of flutter, as shown in [35]. In fact, the predicted flutter bounds with aerodynamic damping are slightly postponed as compared to the case without damping. On average, the flutter pressure parameter is increased by 0.7% and 6.3% for $\mu/M_\infty = 0.01$ and 0.1, respectively. However, since the impact of the aerodynamic damping on the flutter bounds is not highly significant, particularly for lower ratios of μ/M_∞, it will be disregarded in the subsequent flutter analyses concerning the assessment of the models predictive capabilities. Actually, the aerodynamic damping will only be taken into account again in the dynamic aeroelastic analysis in the time domain. As regards to active flutter control, some preliminary conclusions can be drawn from Table 2. Referring to the SC conditions as standpoint, the use of positive control gains increases the flutter bound, which in turn enhances the supersonic flutter resistance of the panel. Conversely,

Table 3
Nondimensionalized flutter dynamic pressure parameters $\tilde{\lambda}_F$ of a smart composite panel with unidirectional fibres of 0°: comparison with available literature solutions.

Model	SC	$G_p = 27.9822$
Song et al. [5]	542.0	789.0
RR CLPT	542.0	789.0
LW FSDT	542.0	789.0
LW F/T/F	541.2	788.6
LW TSDT	541.2	788.6

the negative control gains have the opposite effect. Therefore, only positive proportional control gains are explored for improving the aeroelastic flutter stability.

To ensure the validation of the FE and RR models with available literature solutions, Table 3 presents the active flutter control results of a (simply supported) smart composite panel with unidirectional fibres of 0° and piezoelectric face layers, in line with Song et al. [5]. The original test case consists of a square plate with in-plane dimensions $a = b = 0.1$ m and total thickness $h = 0.0012$ m (each piezoelectric layer with 0.0001 m of thickness), under supersonic airflow along the x-axis. Moreover, Song et al. [5] also make use of a Rayleigh–Ritz CLPT model with trigonometric expansion functions (including both membrane and bending deformations). In accordance with [5], the aerodynamic damping is included, assuming $\mu/M_\infty = 0.1$, and the nondimensionalized flutter pressure parameter is given by $\tilde{\lambda} = \lambda a^3/D_1$, with $D_1 = E_1^c h_c^3/(12(1-\nu_{12}^c\nu_{21}^c))$. The solutions are reported for both SC conditions and active control conditions with proportional gain $G_p = 27.9822$ (which leads to the maximum flutter resistance according to the optimization study presented in [5]). As perceived from Table 3, the present FE and RR solutions are in excellent agreement with the benchmark results reported by Song et al. [5], thus validating the developed models.

Nevertheless, it is worth mentioning that comprehensive assessments of the proposed LW models for the analysis of purely elastic composite laminates and soft core sandwich panels are provided in previous works by the authors [29,36], including a comparison with available literature solutions regarding both refined FE models and 3D exact solutions.

5.2. Active flutter control of VSC panels with piezoelectric layers

The detailed assessment of the LW models predictive capabilities in active aeroelastic flutter control analysis of smart curvilinear fibre composite panels fully covered by piezoelectric layer is presented in Tables 4–6, considering airflow along the x-axis ($\Lambda = 0°$) and various side-to-thickness ratios. As intended, when dealing with thin panels, the results obtained using the proposed LW models are compared with RR CLPT solutions. In particular, for the smart CSC laminate with unidirectional fibres of 0° or 90° (i.e. without bending–twisting coupling), the RR CLPT solutions are derived resorting to trigonometric series expansions. For the remaining laminates, which are inherently characterized by a pronounced bending–twisting coupling behaviour, due to the variable fibre angle distributions, it is considered Legendre polynomials as expansions functions. Despite of the adopted expansion type, ten terms are considered in each in-plane direction to ensure converged solutions.

In Tables 4–6 it is considered either SC conditions or active control conditions with $G_p = 5$, 15 and G_p^*, where G_p^* stands for the control gain that leads to the maximum flutter resistance of each composite laminate when considering panels with $a/h = 250$. According to Fig. 4, the maximum flutter pressure parameter of the panels with $a/h = 250$ under supersonic airflow with $\Lambda = 0°$ is achieved when considering: (i) $G_p = 31$ for the smart cross-ply laminate; (ii) $G_p = 25$ for the smart *VSC1* laminate; and (iii) $G_p = 17$ for the smart *VSC2* laminate. The previously mentioned control gains lead to relative increases of 28%, 52% and 101%, respectively, with respect to the flutter pressure parameter of the corresponding uncontrolled system. Note that for $\Lambda = 0°$, the evolution of the flutter pressure parameter with the proportional control gain of the smart cross-ply laminate has a plateau between $G_p = 31$ and 42. It is interesting to highlight that in between this values, the flutter pressure parameter and the flutter frequency remain constant. For $G_p > 42$, flutter starts to emerge at lower dynamic pressure parameters, but at the same frequency. In contrast, the flutter pressure parameter curves associated with the curvilinear fibre composites do not show any constant plateau.

Fig. 4 includes not only the case of airflow along the x-axis ($\Lambda = 0°$), but also the case of yawed airflow with $\Lambda = 45°$ to further characterize the aeroelastic response behaviour of the laminates and the impact of the active proportional control. For yaw angle $\Lambda = 45°$, the maximum flutter resistance of the panels with $a/h = 250$ is obtained with the following control gains: (i) $G_p = 15$ for the smart cross-ply laminate ($\tilde{\lambda}_F = 1046.3$); (ii) $G_p = 9$ for the smart *VSC1* laminate ($\tilde{\lambda}_F = 1482.0$); and (iii) $G_p = 13$ for the smart *VSC2* laminate ($\tilde{\lambda}_F = 1255.1$). The aforementioned flutter pressure parameters are obtained using the LW TSDT model and correspond to relative increases of 88%, 66% and 71%, respectively, with respect to the uncontrolled system. Regarding the flutter frequency, it is worth mentioning that for SC conditions, flutter occurs due to the first two modes (for all stacking sequences considered) and as the control gain increases, flutter starts to emerge due to the third and fourth modes. Nonetheless, the smart cross-ply laminate also shows flutter due to the second and third modes when the maximum flutter resistance is achieved. In particular, there is a discrepancy between the LW FSDT model and the high-order LW models in this region where flutter occurs due to the second and third modes. The LW FSDT model predicts that this region appears for control gains ranging between $G_p = 14$ and 17, while the LW F/T/F and LW TSDT models estimate that it is only starts for $G_p = 15$ (see the bottom right plot of Fig. 4).

In Fig. 4, the evolution of the flutter pressure parameter with the proportional gain is explained by the modes involved in the occurrence of flutter. As shown in Figs. 6 and 7, the coalescence of natural frequencies is significantly influenced by the applied control gain, which is either delayed or anticipated, leading to different flutter bounds. In fact, for values of control gain around the value that leads to the maximum flutter resistance, there is a change in the modes that lead to flutter (usually from the first two modes to high-order modes), as also perceived by the jump in the flutter frequency.

Since the flutter resistance of a multilayered composite panel is highly dependent on the alignment of the outer layers fibres with the airflow direction, the selected curvilinear fibre composite laminates outperform the cross-ply configuration for yawed airflow. Likewise, the smart cross-ply composite laminate has the higher flutter resistance for airflow along the x-axis.

Regarding the flutter pressure parameters of the smart cross-ply laminate, a careful examination of the results given in Table 4 reveals that the maximum discrepancy of the RR CLPT solutions with respect to the LW TSDT model is 0.3% and 1.7% for $a/h = 250$ and 100, respectively. Likewise, the corresponding discrepancies for the smart *VSC1* laminate are 0.7% and 6.3% (Table 5), whereas for the smart *VSC2* laminate, are 30% and 2.3% (Table 6) for $a/h = 250$ and 100, respectively.

Actually, the highest discrepancy between the RR CLPT solutions and the FE solutions occurs for the smart *VSC2* laminate, when considering $a/h = 250$ and SC conditions (where flutter arises among the seventh and eighth modes). In this particular case, the RR CLPT model may need more expansion functions in-plane to accurately predict the coalescence of the seventh and eighth natural frequencies. Nonetheless, transverse shear deformation effects are more relevant in high-order modes and, therefore, an accurate estimation of the flutter bound involving the seventh and eighth modes may require the inclusion of transverse shear (which is neglected in the CLPT). As a matter of

Table 4
Nondimensionalized flutter dynamic pressure parameters $\tilde{\lambda}_F$ and flutter frequencies f_F (Hz) of the (PZT-4/0/90/0/PZT-4) smart *CSC* laminated panel under supersonic airflow along the x-axis ($\Lambda = 0°$).

	Model	$a/h = 250$		$a/h = 100$		$a/h = 50$		$a/h = 25$	
		$\tilde{\lambda}_F$	f_F	$\tilde{\lambda}_F$	f_F	$\tilde{\lambda}_F$	f_F	$\tilde{\lambda}_F$	f_F
SC	RR CLPT	1330.9	52.68	1330.5	131.65	–	–	–	–
	LW FSDT	1328.1	52.63	1314.5	131.10	1269.0	258.99	1122.3	497.19
	LW F/T/F	1327.2	52.62	1309.0	130.93	1249.3	257.72	1067.4	489.72
	LW TSDT	1327.2	52.62	1309.0	130.93	1249.3	257.72	1067.4	489.72
$G_p = 5$	RR CLPT	1367.2	52.92	1366.8	132.25	–	–	–	–
	LW FSDT	1364.8	52.88	1351.6	131.76	1307.4	260.59	1166.1	503.07
	LW F/T/F	1363.8	52.87	1346.4	131.61	1289.3	259.57	1118.7	498.02
	LW TSDT	1363.8	52.87	1346.4	131.61	1289.3	259.57	1118.7	498.02
$G_p = 15$	RR CLPT	1467.7	53.78	1467.3	134.41	–	–	–	–
	LW FSDT	1470.3	53.80	1458.7	134.20	1420.3	266.57	1306.8	525.89
	LW F/T/F	1468.7	53.78	1453.0	134.10	1405.2	266.22	1290.3	531.51
	LW TSDT	1468.7	53.78	1453.0	134.10	1405.1	266.22	1290.1	531.47
$G_p = 31$	RR CLPT	1707.8	67.50[b]	1707.1	168.69[b]	–	–	–	–
	LW FSDT	1703.7	67.45[b]	1684.6	167.98[b]	1620.7	331.62[b]	1418.2	635.01[a]
	LW F/T/F	1702.8	67.45[b]	1679.3	167.88[b]	1602.0	330.95[b]	1276.4	958.08[c]
	LW TSDT	1702.8	67.45[b]	1679.3	167.88[b]	1602.0	330.95[b]	1276.8	958.09[c]

[a] Flutter due to the second and third modes.
[b] Flutter due to the third and fourth modes.
[c] Flutter due to the eighth and ninth modes; otherwise due to the first two modes.

Table 5
Nondimensionalized flutter dynamic pressure parameters $\tilde{\lambda}_F$ and flutter frequencies f_F (Hz) of the (PZT-4/$\langle 0, 45\rangle$/$\langle$-45, -60$\rangle$/$\langle 0, 45\rangle$/PZT-4) smart *VSC1* laminated panel under supersonic airflow along the x-axis ($\Lambda = 0°$).

	Model	$a/h = 250$		$a/h = 100$		$a/h = 50$		$a/h = 25$	
		$\tilde{\lambda}_F$	f_F	$\tilde{\lambda}_F$	f_F	$\tilde{\lambda}_F$	f_F	$\tilde{\lambda}_F$	f_F
SC	RR CLPT	998.4	45.50	998.0	113.71	–	–	–	–
	LW FSDT	996.8	45.48	987.7	113.39	956.8	224.68	853.3	433.90
	LW F/T/F	996.2	45.47	984.6	113.31	946.7	224.15	825.8	430.45
	LW TSDT	996.4	45.47	984.8	113.32	946.9	224.17	825.9	430.46
$G_p = 5$	RR CLPT	1055.6	46.50	1055.2	116.22	–	–	–	–
	LW FSDT	1053.8	46.48	1044.4	115.91	1012.4	229.80	905.5	444.80
	LW F/T/F	1053.0	46.47	1041.0	115.81	1002.0	229.27	878.6	441.61
	LW TSDT	1053.3	46.47	1041.2	115.82	1002.2	229.28	878.8	441.65
$G_p = 15$	RR CLPT	1236.8	50.32	1236.2	125.74	–	–	–	–
	LW FSDT	1234.3	50.29	1224.7	125.52	1192.3	249.67	1087.8	490.58
	LW F/T/F	1232.2	50.24	1218.5	125.27	1178.2	248.76	1064.8	489.24
	LW TSDT	1232.6	50.25	1218.9	125.29	1178.6	248.81	1065.2	489.36
$G_p = 25$	RR CLPT	1527.0	57.17	1525.9	142.86	–	–	–	–
	LW FSDT	1522.7	57.10	1472.4	288.16[b]	1255.1	553.41[b]	1203.3	624.33[a]
	LW F/T/F	1516.3	57.01	1434.2	287.17[b]	1087.7	546.47[b]	1170.8	621.76[a]
	LW TSDT	1516.9	57.02	1434.6	287.15[b]	1088.3	546.42[b]	1170.3	621.75[a]

[a] Flutter due to the third and fourth modes.
[b] Flutter due to the sixth and seventh modes; otherwise due to the first two modes.

fact, the highest discrepancy between the LW FSDT model and the high-order LW models in the analysis of thin panels occurs indeed for the smart *VSC2* laminate panel with $a/h = 250$ and SC conditions. Specifically, the LW FSDT model overpredicts the flutter dynamic pressure parameter in 5% as compared to the LW F/T/F and LW TSDT models, which clearly highlights the necessary inclusion of transverse shear deformations and its accurate modelling in the (variable stiffness) composite core to obtain highly accurate flutter predictions, even when dealing with thin panels.

For the smart *VSC1* and *VSC2* laminated panels with $a/h = 100$, considering $G_p = 25$ and $G_p = 17$, respectively, the discrepancies are due to the different modes that lead to the occurrence of flutter. In fact, the RR CLPT model predicts flutter due to the first two modes, but the LW FE models estimate that flutter arises due to high-order modes.

The overall discrepancies between the RR CLPT solutions and the FE solutions are mostly explained by the absence of transverse shear deformations in the CLPT, which leads to an overestimation of the panels stiffness. Additionally, the proposed FE models make use of LW descriptions, including not only discrete layer transverse membrane/bending deformation effects, but also discrete layer transverse shear deformation effects (thus allowing zig-zag through-thickness distributions of in-plane displacements to be captured, in line with 3D exact static solutions of piezoelectric composite plates in actuation mode [18,19]). On the other hand, the RR CLPT model, which is based on an ESL description, is not capable of predicting displacements with zig-zag through-thickness distributions. Nonetheless, from a purely practical point of view, the majority of the results is in agreement with the FE solutions. Hence, the RR CLPT model may be considered suitable for preliminary analysis and design of smart composite panels. Nonetheless, it should be emphasized once more that: (i) both membrane and bending deformations must be included in the formulation; and (ii) in laminates with bending–twisting coupling, such as any VSC laminate, the Legendre polynomials are preferable to the trigonometric functions for the Rayleigh–Ritz approximations.

Comparing the results given in Tables 4–6, it is perceived that in the case of thin panels with $a/h = 250$ or 100, the three LW models are in very good agreement for most control conditions. Ergo, it is concluded that the LW FSDT model ensures the best compromise

Table 6
Nondimensionalized flutter dynamic pressure parameters $\tilde{\lambda}_F$ and flutter frequencies f_F (Hz) of the (PZT-4/⟨30, 0⟩/⟨45, 90⟩/⟨30, 0⟩/PZT-4) smart *VSC2* laminated panel under supersonic airflow along the x-axis ($\Lambda = 0°$).

	Model	$a/h = 250$		$a/h = 100$		$a/h = 50$		$a/h = 25$	
		$\tilde{\lambda}_F$	f_F	$\tilde{\lambda}_F$	f_F	$\tilde{\lambda}_F$	f_F	$\tilde{\lambda}_F$	f_F
SC	RR CLPT	1003.6	128.96[b]	1097.8	111.90	–	–	–	–
	LW FSDT	812.3	128.88[b]	1088.3	111.81	1060.0	222.85	964.7	439.83
	LW F/T/F	774.2	128.81[b]	1085.9	111.81	1051.1	222.76	936.8	438.29
	LW TSDT	774.4	128.81[b]	1085.8	111.80	1051.1	222.76	936.7	438.27
$G_p = 5$	RR CLPT	1178.9	46.48	1178.3	116.15	–	–	–	–
	LW FSDT	1177.0	46.47	1169.4	116.16	1143.7	232.29	1061.0	465.67
	LW F/T/F	1176.5	46.47	1166.9	116.17	1135.3	232.35	1038.1	466.28
	LW TSDT	1176.4	46.47	1166.8	116.16	1135.2	232.34	1038.0	466.25
$G_p = 15$	RR CLPT	1503.0	56.24	1501.8	140.45	–	–	–	–
	LW FSDT	1500.7	56.24	1504.3	143.03	1485.3	283.24	1131.6	616.60[a]
	LW F/T/F	1496.9	56.08	1497.7	142.39	1477.7	283.22	1086.8	612.24[a]
	LW TSDT	1496.6	56.06	1497.4	142.34	1477.6	283.23	1087.2	612.25[a]
$G_p = 17$	RR CLPT	1558.7	57.10	1558.0	142.71	–	–	–	–
	LW FSDT	1556.1	57.07	1518.5	161.45[a]	1391.0	322.45[a]	1054.8	613.47[a]
	LW F/T/F	1554.0	57.08	1522.2	161.21[a]	1381.5	322.10[a]	1024.2	608.91[a]
	LW TSDT	1553.9	57.08	1522.7	161.20[a]	1382.0	322.09[a]	1024.6	608.93[a]

[a] Flutter due to the third and fourth modes.

[b] Flutter due to the seventh and eighth modes; otherwise due to the first two modes.

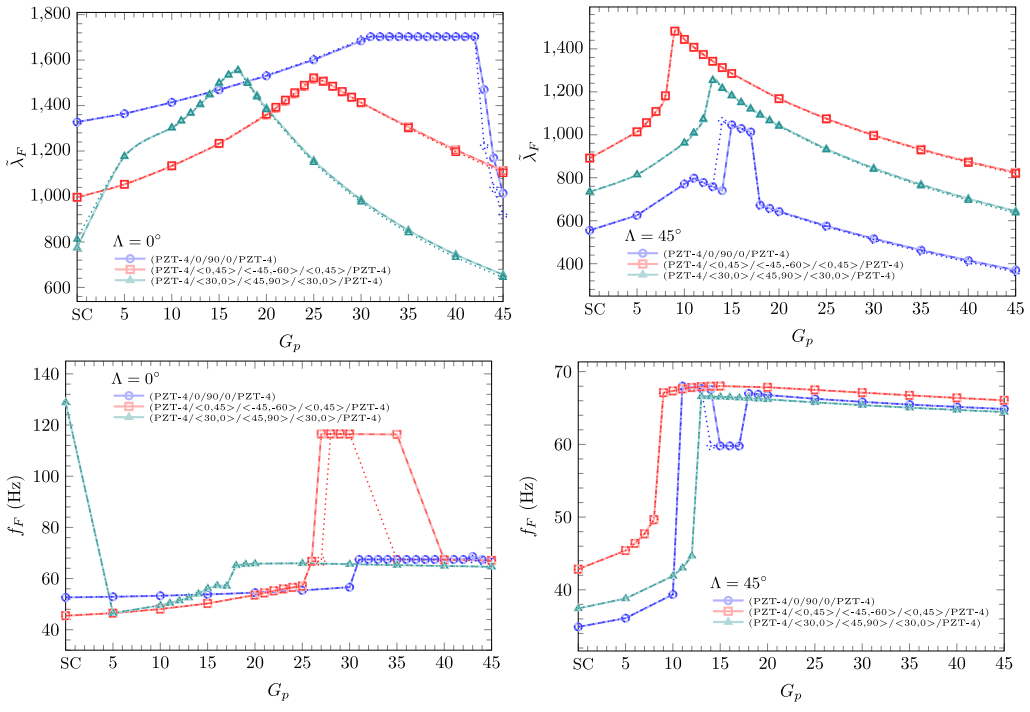

Fig. 4. Evolution of the nondimensionalized flutter pressure parameter $\tilde{\lambda}_F$ and flutter frequency f_F with the proportional control gain G_p of smart composite panels fully covered by piezoelectric layers, with $a/h = 250$: LW FSDT (dotted lines), LW F/T/F (dashed lines) and LW TSDT (solid lines) models.

between numerical accuracy and computational efficiency for active aeroelastic flutter control analysis of thin panels. However, the piecewise first-order model shows some discrepancies when flutter occurs due to high-order modes, such as in the smart *VSC1* laminate with $a/h = 100$ and $G_p = 25$, and smart *VSC2* laminate with $a/h = 250$ and SC conditions. In addition, it can lead to slight deviations in the evolution of the flutter pressure parameter and flutter frequency with the proportional control gain, as shown in Fig. 4.

As regards to the comparison of the proposed LW models in the analysis of moderately thick composite panels, the results provided in Tables 4–6 show that the kinematic refinements introduced in the high-order LW models are indeed useful to achieve accurate flutter solutions. This conclusion is in accordance with the fact that the effect of transverse shear deformations is more significant in the mechanical response of moderately thick panels, as compared to thin counterparts. Accordingly, it is observed that as the side-to-thickness ratio decreases, the discrepancies of the LW FSDT model with respect to the high-order LW models increase. The consistent agreement between the LW F/T/F and LW TSDT models, regardless of the panels side-to-thickness ratio and applied proportional control gain, may be explained by the thin piezoelectric layers considered in the test cases. Since each piezoelectric layer has just 5% of the panel total thickness, the transverse shear deformation effects in the active skins are relatively low, thus being well estimated by the FSDT with unitary shear correction factor as compared to the TSDT (even when considering moderately thick panels with $a/h = 25$). Therefore, it is concluded that the high-order kinematic refinements considered for the piezoelectric face layers in the LW TSDT model render insignificant effects in active aeroelastic flutter control

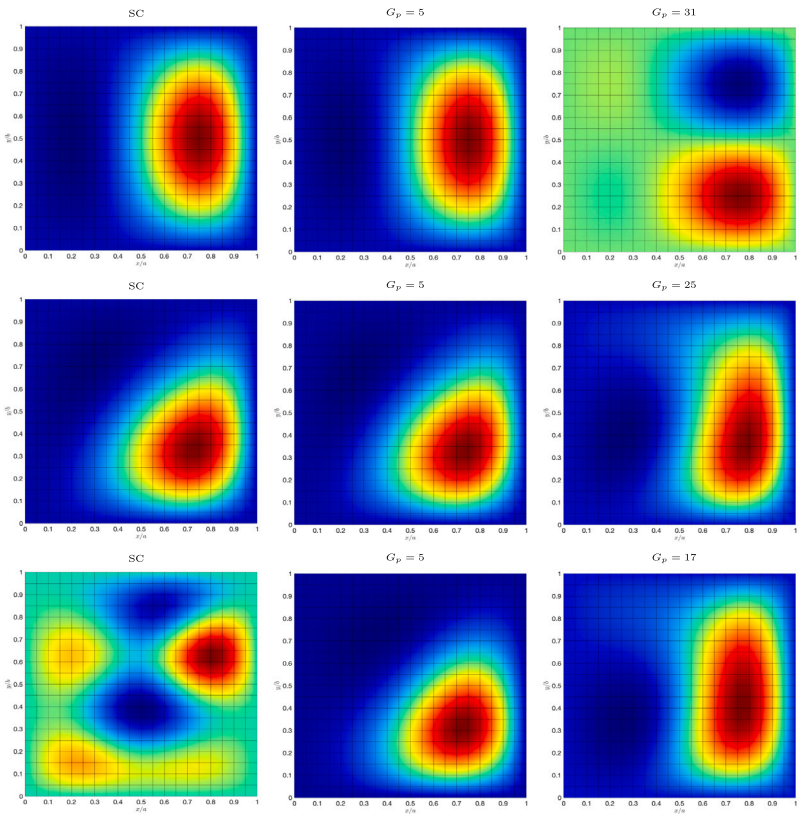

Fig. 5. Flutter in-plane mode shapes $w(x, y, 0)$ of smart composite panels ($a/h = 250$, $\Lambda = 0°$) predicted by the LW F/T/F model: (PZT-4/0/90/0/PZT-4) in the first line, (PZT-4/$\langle 0, 45\rangle$/$\langle$-45, -60$\rangle$/$\langle 0, 45\rangle$/PZT-4) in the second line and (PZT-4/$\langle 30, 0\rangle$/$\langle 45, 90\rangle$/$\langle 30, 0\rangle$/PZT-4) in the third line.

analysis of supersonic smart composite panels with thin piezoelectric sensors and actuators. Actually, for real aerospace applications, the piezoelectric elements should be made as thin as possible to reduce the mass added to the base composite panel.

In Tables 4–6, the smart cross-ply composite laminate with $a/h = 25$ and $G_p = 31$ is the only test case where the LW models differ regarding the modes that lead to the occurrence of flutter. Specifically, the LW FSDT model predicts flutter due to the second and third modes, whereas both LW F/T/F and LW TSDT models estimate the occurrence of flutter due to the eighth and ninth modes. When examining the flutter pressure parameters, it is verified that the discrepancy of the LW FSDT model as compared to the high-order LW models (11%) is higher than for the case where flutter arises in the first two modes (e.g. 5% in SC conditions). Hence, it is pointed out that the kinematic refinements introduced in the high-order LW models, aimed for a better description of the through-thickness distribution of transverse shear deformations and stress, are indeed necessary to obtain highly accurate aeroelastic flutter predictions involving high-order modes, such as the seventh, eight and ninth modes. This result holds not only for moderately thick panels, but also for thin panels, as demonstrated in the case of the smart *VSC2* laminate with $a/h = 250$ and SC conditions (Table 6). However, for moderately thick plates, even when considering flutter among the first four modes, the use of high-order theory, at least for the composite core, appears rather necessary to ensure accurate active aeroelastic flutter control analyses. Note that for panels with $a/h = 25$, showing flutter among the first four modes, the flutter pressure parameters predicted by the LW FSDT model are 3% to 5% higher than the ones obtained making use of the high-order LW models.

A suggestion to improve the accuracy of the LW FSDT model, especially in the analysis of moderately thick plates, would be to consider a non-unitary shear correction factor for the composite layers. Nevertheless, selecting the appropriate shear correction factor is a challenging task as it depends on a plethora of variables, including the geometry, fibre orientations, material properties, as well as boundary and loading conditions. The interested reader can find a comparison of different shear correction factors in a previous work by the authors [29], considering supersonic flutter analysis of purely elastic composite plates with curvilinear fibres.

To provide a further insight in the aeroelastic response behaviour of the various laminates, Fig. 5 presents the flutter in-plane mode shapes of thin panels under supersonic airflow along the x-axis for $\lambda = \lambda_F$. It can be firstly noticed that the mode shapes of the smart cross-ply composite laminate are symmetric/antisymmetric with respect to $y/b = 0.5$, as opposed to the cases of variable stiffness composite laminates with curvilinear fibres, where no type of symmetry is noticed. Additionally, the electrical boundary conditions of the piezoelectric layers (i.e. either SC conditions or active control conditions) and the stacking sequence of the composite core impact significantly the flutter mode shapes. Considering the smart *VSC2* laminate panel, for instance, the flutter mode shape for SC conditions is indeed the one that shows the most complicated distribution of the transverse displacement. This occurs because flutter arises due to the seventh and eight modes. In fact, for $G_p = 5$ and 17, flutter emerges as the first two modes coalesce, leading to flutter mode shapes which are more similar to the remaining ones.

Additionally, Fig. 6 illustrates how the control gain can affect the evolution of the first ten natural frequencies with the nondimensionalized dynamic pressure parameter, taking as an example the smart *VSC1* laminate panel with $a/h = 250$ under airflow along the x-axis. In this example, the coalescence of the first two natural frequencies is successively postponed as the control gain increases, whereas the coalescence of the third and fourth modes as well as the sixth and seventh modes moves backwards. For $G_p = 25$, the maximum flutter resistance is achieved and flutter occurs due to the coalescence of the first two modes (even though the third and fourth modes as well as the sixth and seventh modes coalesce almost immediately after). By further

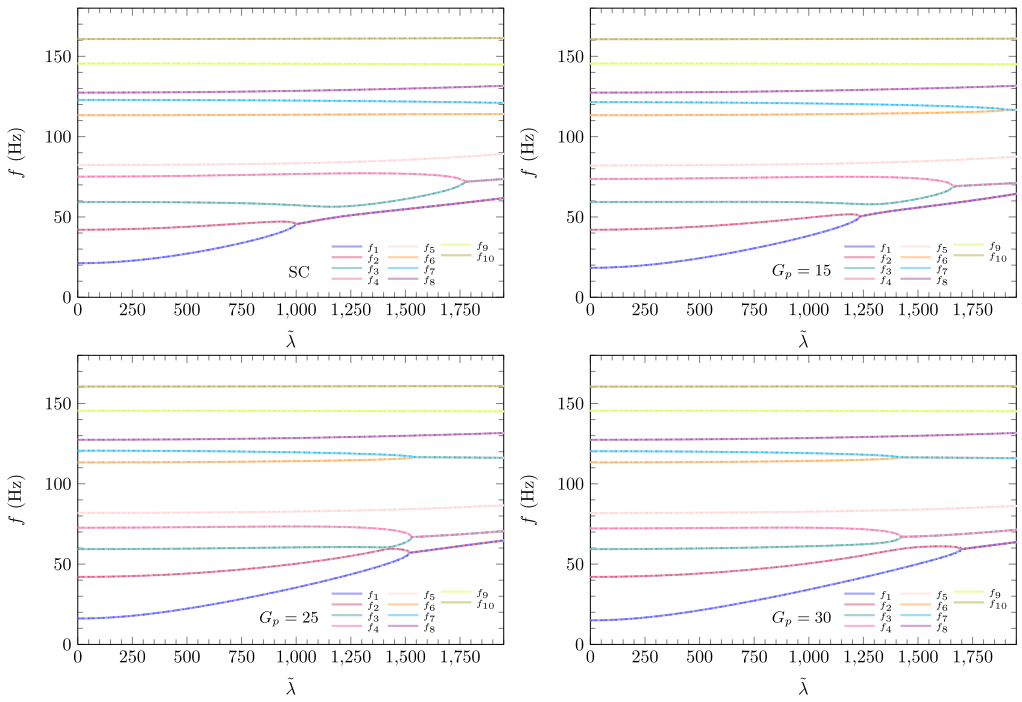

Fig. 6. Variation of the first ten natural frequencies f_n with the nondimensionalized pressure parameter $\tilde{\lambda}$ of the (PZT-4/⟨0, 45⟩/⟨-45, -60⟩/⟨0, 45⟩/PZT-4) smart *VSC1* laminated panel ($a/h = 250$, $\Lambda = 0°$): LW FSDT (dotted lines), LW F/T/F (dashed lines) and LW TSDT (solid lines) models.

increasing the control gain to $G_p = 30$, the flutter resistance is reduced as the coalescence of the sixth and seventh frequencies is the first to occur. In addition, the fifth, eighth, ninth and tenth natural frequencies remain mostly constant throughout the different diagrams.

In Fig. 7, the evolution of the modal damping factors with the nondimensionalized dynamic pressure parameter is also included alongside the natural frequencies, taking now the smart *VSC2* laminate as an example. The diagrams are provided for SC conditions and active control conditions with $G_p = 17$ (which provides the maximum flutter resistance in this test case). As perceived from this figure, the coalescence of natural frequencies occurs when the associated modal damping factors arise as symmetric values (i.e. the eigenvalues are complex conjugated pairs). Note that the aerodynamic damping is neglected in these results and, therefore, the modal damping factors are null prior to flutter.

In line with the trends provided in Fig. 7, flutter occurs due to the seventh and eight modes in the case of SC conditions, as indicated in Table 6. The discrepancies between the LW models, namely the first-order model and the high-order models, regarding the behaviour of these modes are clearly visible in the zoomed portion of the diagram. Moreover, it is also shown that despite the appearance of flutter due to high-order modes, this instability is limited to a quite reduced range of modal damping factors and it vanishes with the increase of the flutter pressure parameter. Nonetheless, as soon as the high-order modes decouple, the first two modes coalesce, giving rise to flutter (once again). On the other hand, for $G_p = 17$, the seventh and eight natural frequencies have very close values for low dynamic pressure parameters, but they get further apart as this parameter increases. In fact, the zoomed portion of the damping diagram for $G_p = 17$ shows that flutter occurs due to the first two modes, though it is immediately followed by the unstable coupling of the third and fourth modes. In this case, some discrepancies between the LW FSDT and the high-order LW models can also be identified, regarding the damping factors of either the first two modes or the third and fourth modes. Specifically, the LW FSDT model predicts a later coupling of the first two damping factors and underestimates the coupling of the third and fourth modes. Hence, the need for refined models capable of accurately predicting both in-plane and transverse shear stress responses is further emphasized, even when dealing with thin smart panels.

In short, the main advantage of the proposed LW models is the inclusion of discrete layer effects, namely in the piezoelectric layers, thus allowing for the prediction of in-plane displacements with zig-zag through-thickness distributions, as shown by 3D electro-elastic solutions of simply supported plates [18,19]. Moreover, the present LW descriptions ensure the proper modelling of the different material properties across the thickness of the smart panels, while considering variable-order shear deformation theories to better predict the actual aero-electro-elastic response, including displacements, in-plane normal stresses and transverse shear stresses. In contrast, pure ESL descriptions of smart composite panels with piezoelectric layers cannot capture in-plane displacements with zig-zag through-thickness distributions, which are especially relevant for the accurate evaluation of the stresses, and may even lead to significant discrepancies when considering high inhomogeneity of material properties between the layers of the laminated composite core and the piezoelectric elements. Furthermore, compared to classical and first-order plate theories, high-order theories provide a more accurate prediction of the through-thickness distributions of the transverse shear stresses [9,24,27]. This feature is particularly important when dealing with moderately thick panels (Tables 4 to 6) or flutter caused by high-order modes (Fig. 7). However, the highly accurate LW models with high-order theories require an increased computational cost as compared to ESL descriptions with CLPT and first-order LW models (which are more suitable for preliminary analysis and design purposes). Actually, the absence of transverse shear deformations is one of the main limitations of the simple and computationally efficient CLPT, leading to an overestimation of the overall stiffness of the panels. Due to the scope of the present work at this stage, it is not included any comparison of structural models regarding stress analysis, but it is highlighted as rather necessary for future works, especially when addressing the non-linear post-flutter regime and failure analysis.

To conclude the detailed analysis of panels fully covered by piezoelectric layers, the aeroelastic response analysis in the time domain is

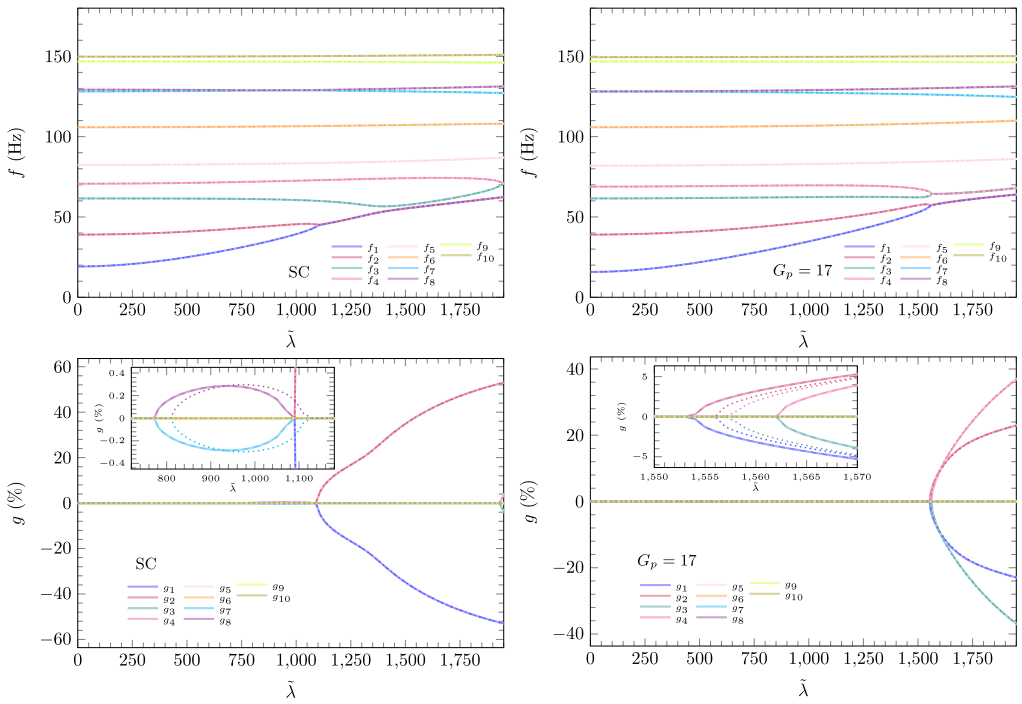

Fig. 7. Variation of the first ten natural frequencies f_n and damping factors g_n(%) with the nondimensionalized pressure parameter $\tilde{\lambda}$ of the (PZT-4/⟨30, 0⟩/⟨45, 90⟩/⟨30, 0⟩/PZT-4) smart *VSC2* laminated panel ($a/h = 250$, $\Lambda = 0°$): LW FSDT (dotted lines), LW F/T/F (dashed lines) and LW TSDT (solid lines) models.

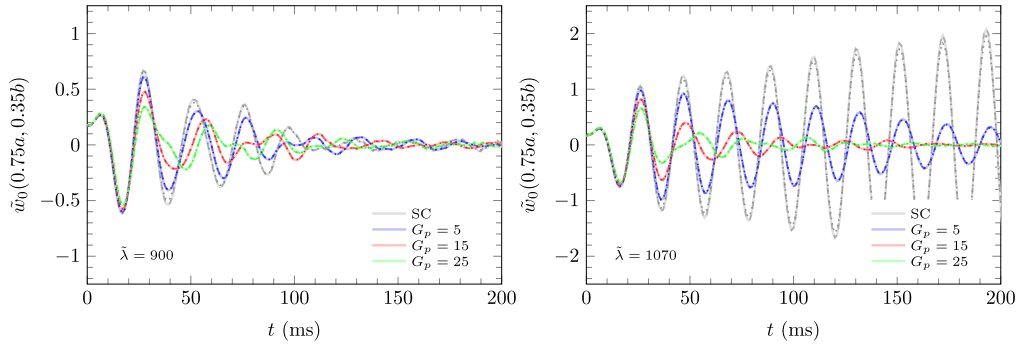

Fig. 8. Time response of the nondimensionalized transverse displacement $\tilde{w}_0(0.75a, 0.35b)$ of the (PZT-4/⟨0, 45⟩/⟨-45, -60⟩/⟨0, 45⟩/PZT-4) smart *VSC1* laminated panel ($a/h = 250$, $\Lambda = 0°$), considering various proportional control gains G_p: LW FSDT (dotted lines), LW F/T/F (dashed lines) and LW TSDT (solid lines) models.

presented in Fig. 8, considering the smart *VSC1* laminate with $a/h = 250$. The panel is initially subjected to an applied bi-sinusoidal load, with a unit peak value, having the surface electrodes in SC conditions. Then, it is released from rest into a medium with supersonic flow along the x-axis and the active control system is engaged. The monitored transverse displacement is evaluated at the absolute maximum in-plane location and it is provided in the following nondimensionalized form $\tilde{w} = 100E_0h^3w/(q_0a^4)$, with $E_0 = 7$ GPa. The aerodynamic damping is included, being estimated in accordance with Eq. (11), assuming $\mu/M_\infty = 0.1$.

The time response analysis of the transverse displacement is carried out for two values of $\tilde{\lambda}$, namely $\tilde{\lambda} = 900$ and $\tilde{\lambda} = 1070$, i.e. prior and after the flutter bound of the panel with SC conditions (the flutter pressure parameters predicted by the LW FSDT model, including aerodynamic damping, can be found in Table 2). The adopted time step in the Newmark method is $\Delta t = 0.001$ s. In the right-hand side of Fig. 8, the aeroelastically unstable response of the uncontrolled system, which shows divergent oscillations, clearly contrasts with the stable response of the controlled systems with active proportional control. Thus further highlighting the capability of the active control technology to improve the aeroelastic stability of supersonic composite panels. It can also be perceived that as the control gain increases, the maximum amplitude of the oscillations is decreased and the initial perturbation is attenuated more quickly. This behaviour is of particular interest to reduce stress levels and minimize fatigue damage. Comparing the LW models, it is concluded that the first-order model predicts slightly lower deflections, which are especially noticeable in the divergent system (i.e. for $\tilde{\lambda} = 1070$ and SC conditions). Nonetheless, from a practical standpoint, the models are considered to be in good agreement among each other.

Since the focus of the present work, at this stage, is merely on the assessment of the proportional control strategy/gain for aeroelastic control, the time response of the applied electric potential on the actuator layer is not included for brevity. Nonetheless, for future works, it is important to note that monitoring the electric potentials of the sensor and actuator layers should be included for a more comprehensive aero-electro-elastic analysis of the smart panels. Moreover, as regards the post-flutter regime shown for SC conditions on the right-hand side of Fig. 8, it is important to note that the linear framework used in this study does not account for the non-linear behaviour of the post-flutter regime. In fact, it is expected that due to the presence of non-linearities in the aeroelastic system, the post-flutter regime is

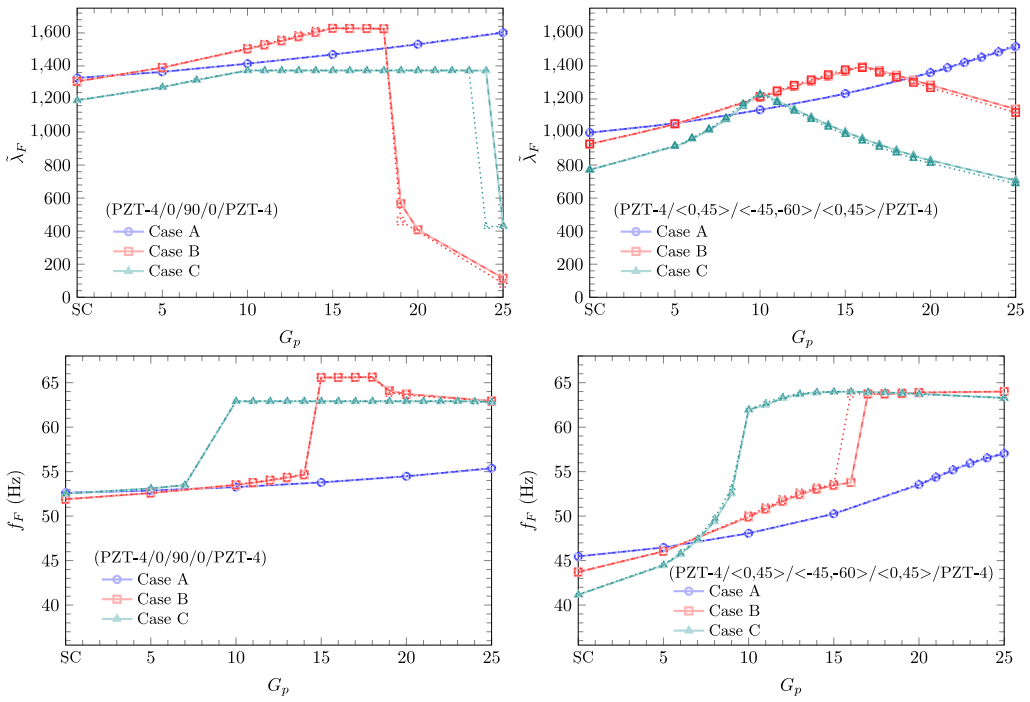

Fig. 9. Evolution of the nondimensionalized flutter pressure parameter $\tilde{\lambda}_F$ and flutter frequency f_F with the proportional control gain G_p of smart composite panels, considering Cases A, B and C ($a/h = 250$, $\Lambda = 0°$): LW FSDT (dotted lines), LW F/T/F (dashed lines) and LW TSDT (solid lines) models.

not actually divergent, but instead ends up as a Limit Cycle Oscillation (LCO) characterized by large vibrations of constant amplitude [46–48].

As far as the aeroelasticity of supersonic panels is concerned, it is worth mentioning that in addition to flutter instability (involving unstable dynamic motion), the study of static aeroelastic instability, known as divergence, is also an important aspect to consider. In fact, the divergence of supersonic panels (i.e. the occurrence of a mode with zero natural frequency) was verified by Moreira et al. [41] when considering smart panels with high values of proportional control gain under low dynamic pressures. However, in the present test cases, divergence instability was never observed for the assumed range of proportional gains, leading to the conclusion that the divergence bound, if it exists, is higher than the flutter bound.

5.3. Active flutter control of VSC panels with multiple piezoelectric patches

Mass is a crucial aspect in aerospace design as it directly affects the structural components from an engineering point of view. As a matter of fact, piezoelectric materials with high actuation levels, such as the piezoceramic PZT-4 considered in this work, tend to have a quite high specific mass (density) as compared to most of the metal and fibre reinforced composites considered for aerospace structures. Therefore, it is essential to optimize the design and placement configurations of the piezoelectric sensors and actuators to ensure feasible active aeroelastic control applications. Considering thin laminates with $a/h = 250$, Fig. 9 presents the evolution of the flutter dynamic pressure parameter and flutter frequency of two configurations with a total of six strips of piezoelectric patches, represented in Fig. 3 as Cases B and C, alongside with the previous solutions for a fully covered panel (Case A). For brevity, it is assumed airflow along the x-axis ($\Lambda = 0°$) and the smart *VSC2* is not included in this final analysis. It is worth noting that the mass saving in terms of piezoelectric material of both Case B and Case C as compared to Case A is 52%.

From the structural modelling point of view, the three LW models are in good agreement for the vast majority of control gains considered in the assessment (as expected since it is considered thin panels). Nonetheless, as previously noticed for fully covered panels, some discrepancies occur between the first-order model and the high-order models when dealing with specific values of control gain. To be precise, for the smart cross-ply laminate, considering both Cases B and C, these discrepancies are noticed in the nondimensionalized flutter pressure parameter when the flutter resistance is in the decreasing zone (i.e. for high values of control gain). On the other hand, for the smart composite laminate with curvilinear fibres, the discrepancies can only be perceived in the flutter frequencies of Case B, for $G_p = 16$. In fact, for this last case, the LW FSDT model predicts that flutter occurs due to the third and fourth modes, whereas the high-order models (LW TSDT and LW F/T/F) estimate that flutter arises as the first two natural frequencies coalesce.

Comparing the configurations with six strips of piezoelectric patches, the case with the patch strips aligned with the airflow direction (Case B) has an overall higher flutter stability than the case with the patch strips perpendicular to the airflow direction (Case C). This may be explained by the fact that the flutter response for $\Lambda = 0°$ is highly dependent on the axial material resistance along the x-axis. Since the added stiffness of Case B, whether purely elastic or induced from active proportional control, is primarily distributed along the x-axis, it has an advantageous impact for improving the flutter resistance. Hence, it is concluded that the control authority in Case B is higher than in Case C.

Overall, for the cases with six patch strips, the maximum flutter resistance occurs for a lower proportional control gain than in the case of the fully covered panel. Considering the Case B and taking the SC conditions as reference: (i) the flutter bound of the smart cross-ply laminate is increased by 25% for $G_p = 15$ (flutter due to the third and fourth modes instead of the first two as in SC conditions); and (ii) the flutter bound of the smart *VSC1* laminate is remarkably improved by 50% for $G_p = 16$ (flutter due to the first two modes, as in SC conditions). Likewise, in the Case C: (i) the flutter bound of the smart cross-ply laminate is increased by 15% for $G_p = 10$ (flutter due to the third and fourth mode, as in SC conditions); and (ii) the flutter bound of the smart *VSC1* laminate is greatly improved by 59% for $G_p = 10$ (flutter due to the third and fourth modes instead of the first two as in SC conditions). Thus, it is also concluded that when considering the control gain that renders the maximum flutter resistance, the modes that lead to the

Table 7
Nondimensionalized flutter pressure parameter $\tilde{\lambda}_F$ and flutter frequency f_F of smart composite panels with six piezoelectric patch strips (results obtained using the LW F/T/F model).

		Case B			Case C		
		$\tilde{\lambda}_F$	f_F	$\delta_{\tilde{\lambda}_F}(\%)$	$\tilde{\lambda}_F$	f_F	$\delta_{\tilde{\lambda}_F}(\%)$
CSC	SC	1306.5	51.89	−2	1191.8	52.52	−10
	$G_p = 10$	1502.6	53.50	6	1372.2	62.90	−3
	$G_p = 15$	1627.7	65.58	11	1372.2	62.90	−7
VSC1	SC	927.5	43.71	−7	771.1	41.15	−23
	$G_p = 10$	1210.1	49.90	7	1229.9	61.96	8
	$G_p = 16$	1394.9	53.78	10	961.6	63.98	−24

$\delta_{\tilde{\lambda}_F}(\%) = (\tilde{\lambda}_F - \tilde{\lambda}_F^{\text{Case A}}) \times 100/\tilde{\lambda}_F^{\text{Case A}}$

occurrence of flutter may not change with respect to the case of SC conditions. Nevertheless, the flutter frequency diagrams represented in Fig. 9 show that around the control gain that leads to the maximum flutter pressure parameter, there is a tendency to occur a jump in the frequency value, which is commonly associated with a change in the modes involved in the occurrence of flutter.

Table 7 provides some detailed results taking into account the LW F/T/F model. Both SC conditions and active control conditions with selected control gains are considered. The control gains are actually chosen such that the maximum flutter pressure parameter of both configurations with six patch strips are presented for each laminate. The relative difference in flutter dynamic pressure parameter of Cases B and C with respect to Case A is also included for comparison purposes.

When considering the configuration of Case B, the flutter resistance for SC conditions is slightly reduced as compared to Case A. However, for some control gains above $G_p = 5$ (see Fig. 9), the flutter pressure parameters of Case B are higher than those of Case A (even though it is considered 52% less mass and surface coverage of piezoelectric material). As regards to Case C, there is no superior flutter resistance for the smart cross-ply laminate. For the smart *VSC1* laminate, the response of Case C only surpasses the one of Case A for control gains around $G_p = 10$.

Overall, the aforementioned results highlight the aeroelastic design optimization of smart composite panels with piezoelectric patches as paramount to achieve improved dynamic and aeroelastic characteristics, while maintaining an optimal and feasible structural mass. Furthermore, the use of variable stiffness composites with curvilinear fibre paths offers, from a design standpoint, an extended tailor-ability as regards to the stiffness distribution, which is highly suitable to be explored in various aeroelastic applications.

6. Conclusions

In this work, variable-order LW shear deformation models are developed for the coupled aero-electro-elastic active flutter control analysis of supersonic smart variable stiffness laminated composite panels with curvilinear fibre paths and surface bonded piezoelectric sensor and actuators layers/patches. It is assumed a LW variable description involving three discrete layers, making use of the FSDT and TSDT, which have not yet been explored to such extent in the literature, thus pushing forward on the study and application of the proper structural modelling for active aeroelastic control analysis of smart curvilinear fibre composite panels. Furthermore, the First-order Piston Theory is adopted to describe the aerodynamic loading resulting from the supersonic airflow, whereas the close loop control law is established resorting to proportional gain. Numerical applications are provided for the accuracy assessment of the proposed models predictive capabilities, including a comparison with Rayleigh–Ritz solutions. Particularly, it is considered simply supported piezoelectric composite panels with either unidirectional or curvilinear fibres, as well as various side-to-thickness ratios and control conditions. Moreover, the proportional control effect on the aeroelastic flutter response is discussed taking into account both airflow along the x-axis and yawed airflow, in addition to three different placement configurations of the piezoelectric patches.

As far as the active aeroelastic control of thin panels is considered, it is concluded that the LW FSDT model ensures the best trade-off between numerical accuracy and computational efficiency. Nonetheless, it is important to note that when dealing with panels that experience flutter due to high-order modes, discrepancies may arise, as demonstrated in variable stiffness configurations under certain control conditions. Furthermore, for the analysis of moderately thick panels, high-order LW models emerge as rather necessary to properly capture the significant impact of transverse shear deformations on the aeroelastic flutter response, especially in the composite core layers. In fact, applying kinematic refinements in the in-plane displacements through-thickness distributions of the composite core alone (as in the LW model with TSDT for the core and FSDT for the piezoelectric face layers) renders highly accurate solutions as compared to the fully refined model (LW TSDT), for both thin and moderately thick panels.

In terms of aeroelastic flutter response behaviour, the active flutter control technology involving proportional control can be used to effectively postpone the flutter bound of composite panels under both airflow along the x-axis and yawed airflow. Additionally, the proportional control gain can alter the modes that lead to flutter and the resulting flutter mode shape. All in all, the combined application of carefully tailored curvilinear fibre paths and optimized piezoelectric sensors and actuators presents a powerful approach for aeroelastic control of advanced and multifunctional supersonic smart panels, offering a wide range of feasible design variables that can be used to solve complex multiobjective design optimization problems. Ultimately, this work provides valuable insights into the advanced modelling and analysis of smart variable stiffness laminated composite panels, which may allow further ensuing research, namely on the aeroelastic design optimization of smart aerospace structures, as well as on the active aeroelastic control of non-linear post-flutter vibrations and fatigue damage/failure prevention. The inclusion of more complex geometries, such as curved panels and shells, and varying boundary conditions are also emphasized as rather important for future research.

CRediT authorship contribution statement

J.A. Moreira: Writing – review & editing, Writing – original draft, Visualization, Validation, Software, Resources, Project administration, Methodology, Investigation, Funding acquisition, Formal analysis, Data curation, Conceptualization. **F. Moleiro:** Writing – review & editing, Supervision, Project administration, Methodology, Funding acquisition, Conceptualization. **A.L. Araújo:** Writing – review & editing, Supervision, Methodology, Funding acquisition, Conceptualization. **A. Pagani:** Writing – review & editing, Supervision, Funding acquisition, Conceptualization.

Declaration of competing interest

The authors declare that they have no known competing financial interests or personal relationships that could have appeared to influence the work reported in this paper.

Data availability

The data that supports the findings of this study is available from the corresponding author upon reasonable request.

Acknowledgements

The authors acknowledge Fundação para a Ciência e a Tecnologia (FCT), Portugal for its financial support via the project LAETA Base Funding (DOI: 10.54499/UIDB/50022/2020). In addition, J.A. Moreira appreciates the financial support of FCT, Portugal through the PhD Grant 2021.06113.BD (DOI: 10.54499/2021.06113.BD). A. Pagani acknowledges funding from the European Research Council (ERC) under the European Union's Horizon 2020 research and innovation programme (Grant agreement No. 850437).

Appendix

This appendix complements the RR CLPT based formulation as proposed originally by Moreira et al. [41] to: (i) employ Legendre polynomial as in-plane expansion functions; and (ii) include membrane deformations. The series expansion of the mid-plane displacements u_0, v_0 and w_0 making use of Legendre polynomials is defined in terms of natural coordinates $\xi = 2x/a$ and $\eta = 2y/b$ as shown:

$$u_0(\xi,\eta,t) = g_2(\eta)\sum_{m=0}^{M}\sum_{n=0}^{N} L_m(\xi)L_n(\eta)q^u_{mn}(t) = \boldsymbol{\Psi}_u^T\boldsymbol{q}_u \tag{A.1a}$$

$$v_0(\xi,\eta,t) = g_1(\xi)\sum_{m=0}^{M}\sum_{n=0}^{N} L_m(\xi)L_n(\eta)q^v_{mn}(t) = \boldsymbol{\Psi}_v^T\boldsymbol{q}_v \tag{A.1b}$$

$$w_0(\xi,\eta,t) = g_1(\xi)g_2(\eta)\sum_{m=0}^{M}\sum_{n=0}^{N} L_m(\xi)L_n(\eta)q^w_{mn}(t) = \boldsymbol{\Psi}_w^T\boldsymbol{q}_w \tag{A.1c}$$

where $L_m(\xi)$ and $L_n(\eta)$ are Legendre polynomials and $g_1(\xi) = (\xi^2 - \xi)$ and $g_2(\eta) = (\eta^2 - \eta)$ in order to satisfy the essential boundary conditions (simply supported). The case of trigonometric expansions, which are considered exclusively for composite layers with unidirectional fibres of 0° or 90°, can be found in Reddy [9]. Moreover, to be consistent with the present FE formulation, the transverse electric field in the RR formulation is written in line with Eq. (7), as opposed to the definition without the minus sign, as originally considered in [41].

The final system of modal aeroelastic equilibrium equations taking into account the active proportional control is derived in a similar fashion to Sections 3 and 4. In the end, the corresponding modal matrices of the RR CLPT model are given by:

$$\boldsymbol{M}_{uu} = \begin{bmatrix} \boldsymbol{M}_{11} & \boldsymbol{0} & \boldsymbol{0} \\ \boldsymbol{0} & \boldsymbol{M}_{22} & \boldsymbol{0} \\ \boldsymbol{0} & \boldsymbol{0} & \boldsymbol{M}_{33} \end{bmatrix} \tag{A.2a}$$

$$\boldsymbol{K}_{uu} = \begin{bmatrix} \boldsymbol{K}_{11} & \boldsymbol{K}_{12} & \boldsymbol{0} \\ \boldsymbol{K}_{12}^T & \boldsymbol{K}_{22} & \boldsymbol{0} \\ \boldsymbol{0} & \boldsymbol{0} & \boldsymbol{K}_{33} \end{bmatrix} \tag{A.2b}$$

$$\boldsymbol{K}^k_{u\phi} = \begin{bmatrix} \boldsymbol{K}^k_{u\phi_1} \\ \boldsymbol{K}^k_{u\phi_2} \\ \boldsymbol{K}^k_{u\phi_3} \end{bmatrix} \tag{A.2c}$$

$$\boldsymbol{K}^k_{\phi\phi} = -\frac{\bar{e}^k_{zz}}{h^k}\mathcal{S}^k \tag{A.2d}$$

such that the modal sub-matrices are obtained as shown:

$$\boldsymbol{M}_{11} = \sum_{k=c,s,a} \rho^k h^k \int_{\mathcal{S}^k} \boldsymbol{\Psi}_u\boldsymbol{\Psi}_u^T dS \tag{A.3a}$$

$$\boldsymbol{M}_{22} = \sum_{k=c,s,a} \rho^k h^k \int_{\mathcal{S}^k} \boldsymbol{\Psi}_v\boldsymbol{\Psi}_v^T dS \tag{A.3b}$$

$$\boldsymbol{K}_{11} = \sum_{k=c,s,a} h^k \int_{\mathcal{S}^k} \bar{Q}^k_{11}\frac{\partial\boldsymbol{\Psi}_u}{\partial x}\frac{\partial\boldsymbol{\Psi}_u^T}{\partial x} + \bar{Q}^k_{16}\left(\frac{\partial\boldsymbol{\Psi}_u}{\partial x}\frac{\partial\boldsymbol{\Psi}_u^T}{\partial y} + \frac{\partial\boldsymbol{\Psi}_u}{\partial y}\frac{\partial\boldsymbol{\Psi}_u^T}{\partial x}\right) + \bar{Q}^k_{66}\frac{\partial\boldsymbol{\Psi}_u}{\partial y}\frac{\partial\boldsymbol{\Psi}_u^T}{\partial y} dS \tag{A.3c}$$

$$\boldsymbol{K}_{12} = \sum_{k=c,s,a} h^k \int_{\mathcal{S}^k} \bar{Q}^k_{12}\frac{\partial\boldsymbol{\Psi}_u}{\partial x}\frac{\partial\boldsymbol{\Psi}_v^T}{\partial y} + \bar{Q}^k_{16}\frac{\partial\boldsymbol{\Psi}_u}{\partial x}\frac{\partial\boldsymbol{\Psi}_v^T}{\partial x} + \bar{Q}^k_{26}\frac{\partial\boldsymbol{\Psi}_u}{\partial y}\frac{\partial\boldsymbol{\Psi}_v^T}{\partial y} + \bar{Q}^k_{66}\frac{\partial\boldsymbol{\Psi}_u}{\partial y}\frac{\partial\boldsymbol{\Psi}_v^T}{\partial x} dS \tag{A.3d}$$

$$\boldsymbol{K}_{22} = \sum_{k=c,s,a} h^k \int_{\mathcal{S}^k} \bar{Q}^k_{22}\frac{\partial\boldsymbol{\Psi}_v}{\partial y}\frac{\partial\boldsymbol{\Psi}_v^T}{\partial y} + \bar{Q}^k_{26}\left(\frac{\partial\boldsymbol{\Psi}_v}{\partial x}\frac{\partial\boldsymbol{\Psi}_v^T}{\partial y} + \frac{\partial\boldsymbol{\Psi}_v}{\partial y}\frac{\partial\boldsymbol{\Psi}_v^T}{\partial x}\right) + \bar{Q}^k_{66}\frac{\partial\boldsymbol{\Psi}_v}{\partial x}\frac{\partial\boldsymbol{\Psi}_v^T}{\partial x} dS \tag{A.3e}$$

$$\boldsymbol{K}^k_{u\phi_1} = \bar{e}^k_{31}\int_{\mathcal{S}^k}\frac{\partial\boldsymbol{\Psi}_u}{\partial x} dS \tag{A.4a}$$

$$\boldsymbol{K}^k_{u\phi_2} = \bar{e}^k_{32}\int_{\mathcal{S}^k}\frac{\partial\boldsymbol{\Psi}_v}{\partial y} dS \tag{A.4b}$$

$$\boldsymbol{K}^k_{u\phi_3} = -\bar{z}^k\int_{\mathcal{S}^k}\bar{e}^k_{31}\frac{\partial^2\boldsymbol{\Psi}_w}{\partial x^2} + \bar{e}^k_{32}\frac{\partial^2\boldsymbol{\Psi}_w}{\partial y^2} dS \tag{A.4c}$$

where $\mathcal{S}^k$ and $\bar{z}^k$ stand for the surface and mid-plane transverse coordinate of the k-layer (note that for the piezoelectric coupling matrices, it is assumed transversely isotropic piezoelectric materials, as considered in the present work). The remaining modal matrices, namely $\boldsymbol{M}_{33}$, $\boldsymbol{K}_{33}$ and $\boldsymbol{K}_{\Delta p}$, are given explicitly in [41]. The surface integrals are obtained analytically resorting to symbolic computation.

References

[1] Shivashankar P, Gopalakrishnan S. Review on the use of piezoelectric materials for active vibration, noise and flow control. Smart Mater Struct 2020;29(5):053001. http://dx.doi.org/10.1088/1361-665x/ab7541.
[2] Araújo AL, Madeira JFA. Multiobjective optimization solutions for noise reduction in composite sandwich panels using active control. Compos Struct 2020;247:112440. http://dx.doi.org/10.1016/j.compstruct.2020.112440.
[3] Moon SH, Hwang JS. Panel flutter suppression with an optimal controller based on the nonlinear model using piezoelectric materials. Compos Struct 2005;68(3):371–9. http://dx.doi.org/10.1016/j.compstruct.2004.04.002.
[4] Nezami M, Gholami B. Optimal locations of piezoelectric patches for supersonic flutter control of honeycomb sandwich panels, using the NSGA-II method. Smart Mater Struct 2016;25(3):035043. http://dx.doi.org/10.1088/0964-1726/25/3/035043.
[5] Song ZG, Li FM, Carrera E, Hagedorn P. A new method of smart and optimal flutter control for composite laminated panels in supersonic airflow under thermal effects. J Sound Vib 2018;414:218–32. http://dx.doi.org/10.1016/j.jsv.2017.11.008.
[6] Asadi D, Farsadi T, Kayran A. Flutter optimization of a wing–engine system with passive and active control approaches. AIAA J 2021;59(4):1422–40. http://dx.doi.org/10.2514/1.J059568.
[7] Kuriakose VM, Sreehari VM. Study on passive flutter control of damaged composite laminates with piezoelectric patches employing finite element method. Compos Struct 2021;269:114021. http://dx.doi.org/10.1016/j.compstruct.2021.114021.
[8] Liew KM, Pan ZZ, Zhang LW. An overview of layerwise theories for composite laminates and structures: Development, numerical implementation and application. Compos Struct 2019;216:240–59. http://dx.doi.org/10.1016/j.compstruct.2019.02.074.
[9] Reddy JN. Mechanics of laminated composite plates and shells – theory and analysis. 2nd ed. Boca Raton: CRC Press; 2004.
[10] Racionero Sánchez-Majano A, Pagani A. Buckling and fundamental frequency optimization of tow-steered composites using layerwise structural models. AIAA J 2023;61(9):4149–63. http://dx.doi.org/10.2514/1.J062976.
[11] Abdalla MM, Setoodeh S, Gurdal Z. Design of variable stiffness composite panels for maximum fundamental frequency using lamination parameters. Compos Struct 2007;81(2):283–91. http://dx.doi.org/10.1016/j.compstruct.2006.08.018.
[12] Lopes CS, Gürdal Z, Camanho PP. Variable-stiffness composite panels: Buckling and first-ply failure improvements over straight-fibre laminates. Comput Struct 2008;86(9):897–907. http://dx.doi.org/10.1016/j.compstruc.2007.04.016.
[13] Stodieck O, Cooper JE, Weaver PM, Kealy P. Improved aeroelastic tailoring using tow-steered composites. Compos Struct 2013;106:703–15. http://dx.doi.org/10.1016/j.compstruct.2013.07.023.
[14] Guimarães TA, Castro SG, Cesnik CE, Rade DA. Supersonic flutter and buckling optimization of tow-steered composite plates. AIAA J 2019;57(1):397–407. http://dx.doi.org/10.2514/1.J057282.
[15] Moita JS, Mota Soares CM, Mota Soares CA. Active control of forced vibrations in adaptive structures using a higher order model. Compos Struct 2005;71(3):349–55. http://dx.doi.org/10.1016/j.compstruct.2005.09.009.

[16] Moita JS, Araújo AL, Martins VM, Mota Soares CM, Mota Soares CA. Analysis of active-passive plate structures using a simple and efficient finite element model. Mech Adv Mater Struct 2011;18(2):159–69. http://dx.doi.org/10.1080/15376494.2010.496062.

[17] Araújo AL, Mota Soares CM, Mota Soares CA. Finite element model for hybrid active-passive damping analysis of anisotropic laminated sandwich structures. J Sandwich Struct Mater 2010;12:397–419. http://dx.doi.org/10.1177/1099636209104534.

[18] Moreira JA, Moleiro F, Araújo AL. Layerwise electro-elastic user-elements in Abaqus for static and free vibration analysis of piezoelectric composite plates. Mech Adv Mater Struct 2022;29(21):3109–21. http://dx.doi.org/10.1080/15376494.2021.1886381.

[19] Moleiro F, Mota Soares CM, Carrera E, Reddy JN. Evaluation of exact electro-elastic static and free vibration solutions of multilayered plates for benchmarking: piezoelectric composite laminates and soft core sandwich plates. Composites C 2020;2:100038. http://dx.doi.org/10.1016/j.jcomc.2020.100038.

[20] Robaldo A, Carrera E, Benjeddou A. A unified formulation for finite element analysis of piezoelectric adaptive plates. Comput Struct 2006;84(22):1494–505. http://dx.doi.org/10.1016/j.compstruc.2006.01.029.

[21] Cinefra M, Carrera E, Valvano S. Variable kinematic shell elements for the analysis of electro-mechanical problems. Mech Adv Mater Struct 2015;22(1–2):77–106. http://dx.doi.org/10.1080/15376494.2014.908042.

[22] Moleiro F, Mota Soares CM, Mota Soares CA, Reddy JN. Layerwise mixed models for analysis of multilayered piezoelectric composite plates using least-squares formulation. Compos Struct 2015;119:134–49. http://dx.doi.org/10.1016/j.compstruct.2014.08.031.

[23] Demasi L, Biagini G, Vannucci F, Santarpia E, Cavallaro R. Equivalent single layer, zig-zag, and layer wise theories for variable angle tow composites based on the generalized unified formulation. Compos Struct 2017;177:54–79. http://dx.doi.org/10.1016/j.compstruct.2017.06.033.

[24] Sánchez-Majano AR, Azzara R, Pagani A, Carrera E. Accurate stress analysis of variable angle tow shells by high-order equivalent-single-layer and layer-wise finite element models. Materials 2021;14(21). https://www.mdpi.com/1996-1944/14/21/6486.

[25] Pagani A, Zappino E, Bracaglia F, Masia R, Carrera E. Thermal stress analysis of variable angle tow composite plates through high-order structural models. Compos Struct 2024;327:117668. http://dx.doi.org/10.1016/j.compstruct.2023.117668.

[26] Yan Y, Liu B, Xing Y, Carrera E, Pagani A. Free vibration analysis of variable stiffness composite laminated beams and plates by novel hierarchical differential quadrature finite elements. Compos Struct 2021;274:114364. http://dx.doi.org/10.1016/j.compstruct.2021.114364.

[27] Moreira JA, Moleiro F, Araújo AL, Pagani A. Assessment of layerwise user-elements in Abaqus for static and free vibration analysis of variable stiffness composite laminates. Compos Struct 2023;303:116291. http://dx.doi.org/10.1016/j.compstruct.2022.116291.

[28] Vescovini R, Dozio L. A variable-kinematic model for variable stiffness plates: Vibration and buckling analysis. Compos Struct 2016;142:15–26. http://dx.doi.org/10.1016/j.compstruct.2016.01.068.

[29] Moreira JA, Moleiro F, Araújo AL, Pagani A. Equivalent single layer and layerwise models for flutter and buckling analysis of supersonic variable stiffness laminated composite plates. Thin-Walled Struct 2023;191:111012. http://dx.doi.org/10.1016/j.tws.2023.111012.

[30] Sánchez-Majano AR, Pagani A, Petrolo M, Zhang C. Buckling sensitivity of tow-steered plates subjected to multiscale defects by high-order finite elements and polynomial chaos expansion. Materials 2021;14(11). https://www.mdpi.com/1996-1944/14/11/2706.

[31] Pagani A, Sánchez-Majano AR. Stochastic stress analysis and failure onset of variable angle tow laminates affected by spatial fibre variations. Composites C 2021;4:100091. http://dx.doi.org/10.1016/j.jcomc.2020.100091.

[32] Pagani A, Racionero Sánchez-Majano A, Zamani D, Petrolo M, Carrera E. Fundamental frequency layer-wise optimization of tow-steered composites considering gaps and overlaps. Aerotecnica Missili Spazio 2024. http://dx.doi.org/10.1007/s42496-024-00212-w.

[33] Carrera E, Zappino E. Aeroelastic analysis of pinched panels in supersonic flow changing with altitude. J Spacecr Rockets 2014;51(1):187–99. http://dx.doi.org/10.2514/1.A32363.

[34] Zappino E, Carrera E, Cinefra M. Aeroelastic analysis of composite pinched panels using higher-order shell elements. J Spacecr Rockets 2015;52(3):999–1003. http://dx.doi.org/10.2514/1.A32986.

[35] Akhavan H, Ribeiro P. Aeroelasticity of composite plates with curvilinear fibres in supersonic flow. Compos Struct 2018;194:335–44. http://dx.doi.org/10.1016/j.compstruct.2018.03.101.

[36] Moreira JA, Moleiro F, Araújo AL, Pagani A. Layerwise models for supersonic flutter analysis of viscoelastic sandwich panels with curvilinear fibre composite skins. J Sound Vib 2024;572:118182. http://dx.doi.org/10.1016/j.jsv.2023.118182.

[37] Fazelzadeh SA, Jafari SM. Active control law design for flutter suppression and gust alleviation of a panel with piezoelectric actuators. Smart Mater Struct 2008;17(3):035013. http://dx.doi.org/10.1088/0964-1726/17/3/035013.

[38] Song Z-G, Li F-M. Active aeroelastic flutter analysis and vibration control of supersonic composite laminated plate. Compos Struct 2012;94(2):702–13. http://dx.doi.org/10.1016/j.compstruct.2011.09.005.

[39] Song Z-G, Li F-M. Aerothermoelastic analysis and active flutter control of supersonic composite laminated cylindrical shells. Compos Struct 2013;106:653–60. http://dx.doi.org/10.1016/j.compstruct.2013.07.029.

[40] Guimarães TA, Rade DA, Cesnik CE. Active flutter suppression on composite tow steered panels based on piezoelectric actuation. In: 59th AIAA/ASCE/AHS/ASC structures, structural dynamics, and materials conference. 2018, https://arc.aiaa.org/doi/abs/10.2514/6.2018-0188.

[41] Moreira JA, Moleiro F, Araújo AL, Pagani A. Analytical modeling of panel flutter and active control in supersonic variable stiffness composite laminates. Mech Adv Mater Struct 2023;30(5):930–44. http://dx.doi.org/10.1080/15376494.2022.2144970.

[42] Wang Z, Chen H, Wang G, Zhang Y, Zheng C. Prediction and active suppression of flutter in composite panel based on eigenvector orientation method. Compos Struct 2021;262:113422. http://dx.doi.org/10.1016/j.compstruct.2020.113422.

[43] Suleman A. Adaptive composites modelling and application in panel flutter and noise suppression. Comput Struct 2000;76(1):365–78. http://dx.doi.org/10.1016/S0045-7949(99)00177-7.

[44] Araújo AL, Lopes HMR, Vaz MAP, Mota Soares CM, Herskovits J, Pedersen P. Parameter estimation in active plate structures. Compos Struct 2006;84:1471–9. http://dx.doi.org/10.1016/j.compstruc.2006.01.017.

[45] Koiter WT. A consistent first approximation in the general theory of thinelastic shells. In: Proceedings of first symposium on the theory of thin elastic shells. Amsterdam: North-Holland; 1959, http://resolver.tudelft.nl/uuid:13cb5366-bbdc-4dd1-8514-951302217759.

[46] Chai Y, Gao W, Ankay B, Li FM, Zhang C. Aeroelastic analysis and flutter control of wings and panels: A review. Int J Mech Syst Dynam 2021;1(1):5–34. http://dx.doi.org/10.1002/msd2.12015.

[47] Dowell EH. Panel flutter - A review of the aeroelastic stability of plates and shells. AIAA J 1970;8(3):385–99. http://dx.doi.org/10.2514/3.5680.

[48] Dowell EH. Nonlinear flutter of curved plates. AIAA J 1969;7(3):424–31. http://dx.doi.org/10.2514/3.5124.

[49] Sciascia G, Oliveri V, Weaver PM. Eigenfrequencies of prestressed variable stiffness composite shells. Compos Struct 2021;270:114019. http://dx.doi.org/10.1016/j.compstruct.2021.114019.